TAMPEREEN TEKNILLINEN YLIOPISTO
TAMPERE UNIVERSITY OF TECHNOLOGY

MARKUS LAATTA

MULTI-GIGABIT WIRELESS COMMUNICATION AT 60 GHz: BEAMFORMING AND MEASUREMENTS

Master of Science Thesis

Examiner: Prof. Mikko Valkama
The examiner and topic of the thesis were approved by the Council of the Faculty of Computing and Electrical Engineering on 9th of November 2016

ABSTRACT

MARKUS LAATTA: Multi-Gigabit Wireless Communication at 60 GHz: Beamforming and Measurements
Tampere University of Technology
Master of Science Thesis, 71 pages
March 2017
Master's Degree Programme in Electrical Engineering
Major: Wireless communications
Examiner: Prof. Mikko Valkama
Keywords: 60 GHz, IEEE 802.11ad, Beamforming, Beam Steering, Antenna Arrays

Usage of wireless communication systems has been growing steadily during the past decades as more and more services and users are starting to utilize various cloud based systems. Need for higher data rates and the exponential increase of users are becoming significant difficulties for the current wireless communication systems. To tackle this problem, frequency bands of several gigahertz have been suggested for the next generation of local and personal communication systems (WLAN/WPAN). The extremely large unlicensed band at 60 GHz is an attractive option to provide multi-gigabit data rates over short distances. However, even at short distances systems have to compensate the poor link budget which is due to increased frequency and bandwidth. To mitigate these losses, highly directional communication with antenna arrays and beamforming is proposed.

IEEE 802.11ad standard is one of the most promising millimeter wave standards to offer multi-gigabit data rates for WLAN/WPAN use. In comparison to the legacy IEEE 802.11 standards, the IEEE 802.11ad introduces completely new medium access control (MAC) and physical (PHY) layers due to highly directional communication.

This thesis studies the IEEE 802.11ad standard, focusing on the renewed MAC and PHY layers, beamforming mechanisms, and overall performance in a home environment. While previous academic work has included measurements at 60 GHz, these measurements have been limited to laboratory and office areas which do not realistically model an actual end-user environment. Additionally, the measurement equipment in these research papers has not explicitly implemented the IEEE 802.11ad standard. Hence, measurements in this thesis are conducted with a prototype implementing the mandatory parts of the standard resulting in a more thorough realization of the performance. The results indicate that the prototype performs well in a home environment. Overall, theoretical PHY data rates of above 2 Gbps are to be expected in most cases if operated in similar environment.

TIIVISTELMÄ

MARKUS LAATTA: Usean gigabitin langaton tiedonsiirto 60 GHz:lla: keilanmuodostus ja mittauksia
Tampereen teknillinen yliopisto
Diplomityö, 71 sivua
Maaliskuu 2017
Sähkötekniikan koulutusohjelma
Pääaine: Langaton tietoliikenne
Tarkastajat: Prof. Mikko Valkama
Avainsanat: 60 GHz, IEEE 802.11ad, Keilanmuodostus, Keilansuuntaus, Antenniryhmä

Langattomien tietoliikennejärjestelmien käyttö on kasvanut tasaisesti viimeisten vuosikymmenten aikana, kun yhä useampi palvelu ja käyttäjä on alkanut käyttää erilaisia pilvipohjaisia järjestelmiä. Tarve suuremmille tiedonsiirtonopeuksille ja käyttäjien eksponentiaalinen kasvu ovat kasvavia haasteita nykyisille langattomille tiedonsiirtojärjestelmille. Ratkaisuksi on ehdotettu uusia useamman gigahertzin taajuuskaistoja langattomille lähi- ja likiverkkoteknologioille. Erittäin laaja lisensioimaton kaista 60 GHz:lla on varteenotettava vaihtoehto tähän käyttöön lyhyillä etäisyyksillä. Taajuuden ja kaistanleveyden kasvaessa ongelmaksi muodostuu heikentyvä linkkibudjetti, minkä kompensoimiseen voidaan käyttää hyvin suuntaavia antenniryhmiä ja keilanmuodostusta.

Usean gigabitin tiedonsiirtonopeuksien saavuttamiseen IEEE 802.11ad on yksi lupaavimmista millimetriaaltostandardeista. Aikaisempiin IEEE 802.11 -standardeihin verrattuna IEEE 802.11ad sisältää kokonaan uuden MAC-kerroksen (medium access control) ja fyysisen kerroksen, mikä johtuu erittäin suunnatuista lähetteistä ja keilanmuodostuksesta.

Tässä työssä tutkitaan IEEE 802.11ad -standardia keskittyen sen uudistettuihin kerroksiin, keilanmuodostusmenetelmiin, ja yleiseen suorituskykyyn kotiympäristössä. Aiemmat tieteelliset julkaisut ovat jo sisältäneet mittauksia 60 GHz:lla, mutta niissä mittausympäristö on rajoittunut laboratorio- ja toimistotiloihin, jotka eivät varsinaisesti vastaa tyypillistä loppukäyttäjän ympäristöä. Tämän lisäksi kyseisissä julkaisuissa käytetty mittalaitteisto ei ole eksplisiittisesti implementoinut standardia. Tässä työssä käytetään koko standardin pakolliset osat implementoivaa prototyyppiä, minkä ansiosta saadaan parempi ymmärrys kyseisen teknologian suorituskyvystä. Tulosten perusteella voidaan sanoa, että prototyyppi suoriutuu hyvin kotiympäristössä. Yleisesti ottaen yli 2 Gbps teoreettiset fyysisen kerroksen tiedonsiirtonopeudet saavutetaan useimmissa tapauksissa, jos toimitaan vastaavassa ympäristössä.

PREFACE

This thesis has been carried out at Intel Corporation as a part of client computing and IEEE 802.11ad research and development.

First of all, I would like to thank Saku Lahti from Intel Corporation for giving me this topic, and making this thesis possible. Moreover, I would like to thank him for his guidance and helpful discussions throughout this process. I am especially grateful for Sami Vaara from Intel Corporation for his valuable comments and relentless guidance which greatly improved the overall quality of the thesis. I would also like to thank Yaniv Michaeli and Jonathan Kosloff from Intel Corporation for their helpful comments regarding the IEEE 802.11ad standard. Special thanks to all my colleagues, whom I had a pleasure to work with, family, and friends for their support during the thesis writing process.

Tampere, 30.12.2016

Markus Laatta

TABLE OF CONTENTS

LIST OF ABBREVIATIONS AND SYMBOLS

5G	Fifth generation
A-BFT	Association beamforming training
ADC	Analog-to-digital converter
AGC	Automatic gain control
ANT	Antenna training field
AP	Access point
ATI	Announcement transmission interval
BHI	Beacon header interval
BI	Beacon interval
BPSK	Binary phase shift keying
BRP	Beam refinement protocol
BTI	Beacon transmission interval
CAD	Computer-aided design
CBAP	Contention-based access period
CEF	Channel estimation field
CEPT	European Conference of Postal and Telecommunications Administrations
CF-End	Contention-free-end
CMOS	Complementary metal-oxide-semiconductor
CSMA/CA	Carrier sense multiple access with collision avoidance
CTS	Clear-to-send
DAC	Digital-to-analog converter
DBPSK	Differential binary phase shift keying
DCF	Distributed coordination function
DL	Downlink
DMG	Directional multi-gigabit
DTI	Data transmission interval
DTS	Denial-to-Send
ECC	European Commission and the Electronic Communications Committee
EDCA	Enhanced distributed channel access
EHF	Extremely high frequency
EIRP	Effective isotropic radiated power

ETSI	European Telecommunications Standards Institute
EVM	Error vector magnitude
FCC	United States Federal Communications Commission
FICORA	Finnish communications regulatory authority
HCF	Hybrid coordination function
IC	Integrated circuit
IF	Intermediate frequency
ISM	Industrial, scientific, and medical (frequency band)
ITU	International Telecommunications Union
LNA	Low noise amplifier
LO	Local oscillator
LOS	Line-of-sight
MAC	Medium access control
MCS	Modulation and coding scheme
MIMO	Multiple input multiple output
NAV	Network allocation vector
NLOS	Non-line-of-sight
OFDM	Orthogonal frequency-division multiplexing
PA	Power amplifier
PAPR	Peak-to-average-power ratio
PBSS	Personal basic service set
PCB	Printable circuit board
PCF	Point coordination function
PCIe	Peripheral Component Interconnect Express
PCP	Personal service set control point
PHY	Physical (layer)
PLL	Phase-locked loop
PP	Polling period
QPSK	Quadrature phase shift keying
RCS	Radar cross section
RF	Radio frequency
R-FEM	Radio front-end module
RFIC	Radio frequency integrated circuit
RSSI	Received signal strength indicator
RTS	Request-to-send
RxSS	Receive sector sweep
SC	Single carrier

SLS	Sector level sweep
SNR	Signal-to-noise ratio
SP	Scheduled service period
SPR	Service period request
STA	IEEE 802.11 station
STF	Short training field
TDMA	Time-division multiple access
TRN-R/T	Receive/Transmit training
TxSS	Transmit sector sweep
UL	Uplink
VCO	Voltage controlled oscillator
WLAN	Wireless local area network
WPAN	Wireless personal area network

A_{eff}	Antenna aperture
B	Bandwidth
c	Speed of light
d	Antenna element spacing
D	Length of an antenna array
$D_{element}$	Length of a single antenna element
e_{max}	Maximum efficiency of an antenna array
E_i	Incident electric field
E_s	Scattered electric field
F	Noise factor
$Ga_N(n)$	Golay sequence of length N
$Gb_N(n)$	
G_r	Receive antenna gain
G_t	Transmit antenna gain
h	Elevation
k	Boltzmann constant
k_0	Wavenumber
P_r	Received power
P_t	Transmitted power
r_n	Radius of nth Fresnel zone
R	Distance
$R_x(k)$	Autocorrelation function of x

S_i	Incident power density
S_s	Scattered power density
T	Temperature
$\delta(k)$	Kronecker delta function
λ	Wavelength
ϕ_n	nth antenna element phase shift
σ_{3D}	Radar cross section
θ	Beam steering angle

1. INTRODUCTION

Recently, research at the 60 GHz frequency band has gained a lot of momentum from industry and academy because of potential multi-gigabit throughputs over short distances. One large driver for this research is the licence-free bandwidth, reaching up to 9 GHz, that was internationally allocated at the 60 GHz band. Even though the spectrum has been available for this purpose in some parts of the globe since the late 1990s, the first low-cost commercial products have been coming out to the market just recently. Important international 60 GHz standards include WirelessHD (2008) [1], ECMA-387 (2008) [2], IEEE 802.15.3c (2009) [3], and IEEE 802.11ad (2012) also known as WiGig [4]. All of these standards are envisioned to be used for personal area and local area networks. The following decades will show which of these will become the de facto standard(s), and whether or not they will have as large commercial success as, for example, the IEEE 802.11 standard has had so far. Indeed, it has been estimated that IEEE 802.11ad chipset shipments will increase sharply in the following years [5, 6].

Due to high atmospheric absorption at 60 GHz, long-range communication at this frequency is not practical. Hence, the spectrum is free for indoor high throughput wireless communication systems where the distances are much shorter. However, even at short distances the systems have to somehow compensate the poor link budget which is due to increased path loss and thermal noise power. As will be shown later in this thesis, the path loss that the signal experiences is related to the signal's wavelength, whereas, the thermal noise power is related to the bandwidth of the system (in this case even as large as 2 GHz). Now, as both of these parameters are higher the losses are respectively also higher. Many of the previously mentioned standards mitigate this fundamental issue by implementing highly directional communication links with antenna arrays and beamforming. Additionally, for the system to be a commercial success, these antenna arrays and baseband implementations need to be inexpensive and preferably low-complex to reduce battery consumption in mobile devices.

1.1 Objectives and Scope of the Thesis

In this thesis, the new amendment to the wireless local area network (WLAN) standard is studied. More precisely, this thesis focuses on the IEEE 802.11ad standard, that is, directional multi-gigabit (DMG) WLAN at 60 GHz. The completely new WLAN band offers significantly more bandwidth than has been available previously in the 2.4 GHz and 5 GHz frequency bands. On the other hand, the 60 GHz band also introduces significant signal attenuation which renders the traditional omni-directional antennas more or less useless. To overcome these drawbacks, highly directional communication is proposed. Therefore, the measurements conducted in this thesis concentrate on the directional communication aspects of the standard, that is, the beam steering and beamforming mechanisms, as well as, the utilized 16-element antenna array.

Previous academic work at 60 GHz has included measurements in laboratory and office areas [7–12]. While these measurements have provided valuable info about the real life signal propagation at 60 GHz, they do not really model a realistic end-user environment. Laboratory and office areas typically do not have the same kind of layouts and obstacles that normal households do. Most end-user devices will be operated at environments that are much more cluttered than the ones in the previously mentioned examples. Therefore, understanding 60 GHz communication in these types of environments becomes increasingly important. As a consequence, measurements conducted in this thesis are done in a home environment.

1.2 Structure of the Thesis

We begin with a short overview of the current state of international spectrum regulation at the 60 GHz frequency band. Next, the general propagation characteristics of millimeter waves are described, again emphasis being on the 60 GHz frequency band. Then, basics of RF and baseband circuits for multi-gigabit millimeter wave communication are introduced, including millimeter wave antenna arrays and beam steering principles. In Chapter 3, The IEEE 802.11ad medium access control (MAC), physical (PHY) layer, and various use cases are described. This includes the specified beamforming mechanisms and protocols of the standard. Measurement methods are described in Chapter 4, including measurement setup and measurement scenario. Measurement results are shown and further analyzed in Chapter 5. Finally, the conclusions are drawn in Chapter 6.

2. MILLIMETER WAVE RADIO FUNDAMENTALS

This chapter addresses the current state of spectrum regulation at millimeter wave bands and also describes the signal propagation characteristics at these frequencies. This is then followed by a short theoretical overview of millimeter wave RF and baseband circuits. Finally, millimeter wave antennas, especially antenna arrays, are examined and fundamentals of antenna array beam steering are described. As this thesis focuses mainly on the IEEE 802.11ad standard, the focus of this chapter is consequently the 60 GHz frequency band.

Research on millimeter waves has an interesting and rich history. The World's first millimeter wave communication system was developed in 1895 by Jagadish Chandra Bose in the Presidency College, Calcutta, India. Bose transmitted and received signals at 60 GHz through two walls at a distance of over 23 meters, detonated some gunpowder and ringed a bell. During his time, Bose invented numerous millimeter wave apparatuses and components. [13]. More recently, militaries around the World have been the pioneers of modern millimeter wave research and earliest military applications emerged during the World War II [14]. Especially during the past decades, the research on millimeter waves has rapidly accelerated, mainly due to the fact that previously these high frequencies have been seen too demanding for the current complementary metal-oxide-semiconductor (CMOS) technologies at reasonable prices [15]. Undoubtedly, the next generation of wireless local area network (WLAN) and wireless personal area network (WPAN) technologies are shifting to the millimeter waves for larger bandwidths and capacity. Similarly, the upcoming fifth generation (5G) cellular network is going to expand cellular communication systems to the millimeter waves [16]. Furthermore, it has also been proposed that the 5G cellular would utilize a heterogeneous network, or HetNet, topology where the IEEE 802.11ad WLAN would coexist with the cellular network and offer traffic off-loading in small cells [17, 18].

2.1 Spectrum Regulation

History has shown us that wireless communication has revolutionary consequences on both human interaction and productivity. Therefore, it is to be expected that more and more applications and use cases are shifting to use wireless communication as the transmission medium. As a consequence, more and more services, data and users are moving to utilize cloud based systems which of course require constant connectivity, meaning that the traditional frequency bands are coming increasingly congested. Need for higher data rates and the exponential increase of users are becoming significant difficulties for the current wireless communication systems. To tackle this problem, frequency bands of several gigahertz have been suggested for the next generation of personal communication systems.

Spectrum regulation at the 60 GHz frequency band was first initialized by the US Federal Communications Commission (FCC) in the early 90s. The original proposition was to establish an unlicensed band to cover frequencies from 59 GHz to 64 GHz, in a similar fashion as the 900 MHz, 2.4 GHz and 5 GHz industrial, scientific and medical (ISM) bands had been regulated earlier [19]. However, the 60 GHz frequency band offers 10 to 100 fold increase in available spectrum. As it is known from the Shannon-Hartley theorem, this equals straight away 10 to 100 fold increase in the channel capacity.

Internationally the most important singular body regarding standardization of radio and telecommunication systems is the International Telecommunications Union (ITU). Even though ITU only publishes recommendations regarding spectrum allocation, they carry significant weight as the ITU is an agency of the United Nations. According to ITU, the $55.78 - 66$ GHz band is recommended to be available for all communication, in other words, for unlicensed use. Furthermore, ITU recommends that this frequency band is to be used for high-density applications for fixed wireless services. [20].

At the European level, the European Commission and the Electronic Communications Committee (ECC) of the European Conference of Postal and Telecommunications Administrations (CEPT) define a framework for the efficient use of radio spectrum within the European Union. Together the participating European countries legislate common policies and non-binding regulations for the European Union member countries. The European Telecommunications Standards Institute (ETSI) is a standardization organization that produces global standards for information and

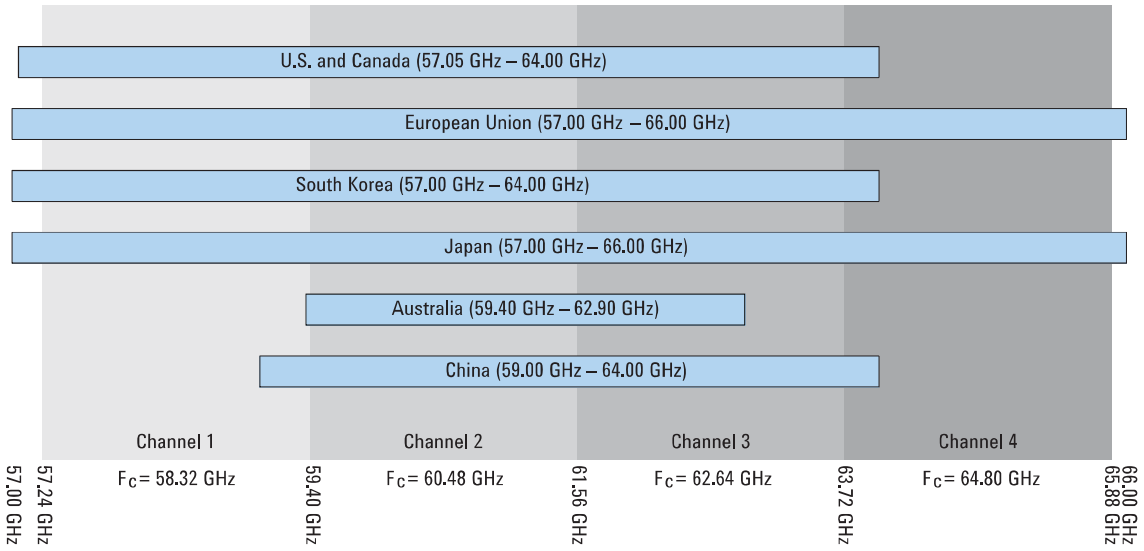

Figure 2.1 *IEEE 802.11ad spectrum allocation and channelization [24].*

communication technologies. These so called harmonized standards are co-produced with the ECC and outline the conformance requirements for communication devices operating at specific parts of the radio frequency spectrum. [21].

In Finland, Finnish communications regulatory authority (FICORA) is the national regulatory body responsible for communication regulations in Finland. As Finland is a member state of the European Union, national regulations comply with the ECC and the ETSI standards. Regulation regarding the frequency band of 57-66 GHz is addressed in the ETSI standard EN 302 567 [22] and redefined by FICORA in Määräys (English: Regulation) 15 AI/2015 M [23]:

- The $57 - 66$ GHz frequency band is intended for license-exempt short-range Wireless Personal Area Network (WPAN) systems operating at multiple Gigabit data rates.
- Effective isotropic radiated power (EIRP) shall not exceed 40 dBm (indoor only) and 25 dBm (indoor and outdoor).
- Maximum spectral power density shall not exceed 13 dBm/MHz (indoor only) and -2 dBm/MHz (indoor and outdoor).
- Fixed outdoor installations are not permitted.

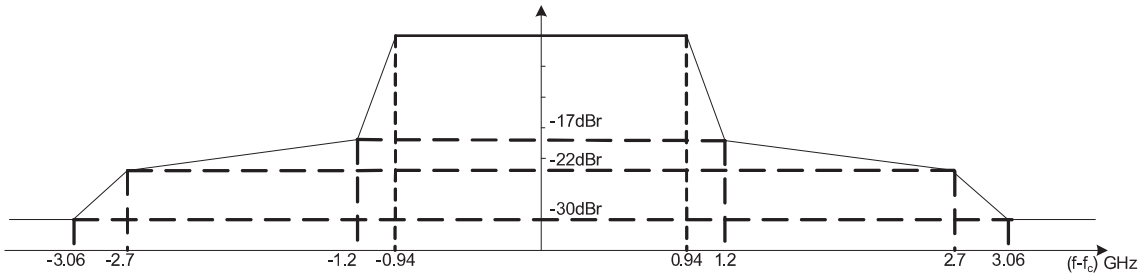

Figure 2.2 *IEEE 802.11ad transmit spectrum mask [4].*

Figure 2.1 summarizes the allocated spectrum and channelization for IEEE 802.11ad at 60 GHz around the world. Each of the four channels is 2.16 GHz wide and as can be seen, not all of them are available globally. Therefore, channel 2 is the default channel for devices operating in this frequency band.

Spectrum mask of an 802.11ad channel is illustrated in Figure 2.2. Note that in the Figure transmit powers are presented relative to the signal level at the carrier frequency. Compared to spectrum masks at lower frequencies, the main difference is the fact that adjacent channel requirements have been noticeably relaxed. This is due to the fact that at 60 GHz circuit level design becomes significantly more challenging.

2.2 Propagation Characteristics

The signal propagation at 60 GHz is often described to be quasi-optical by nature, meaning that the received signal is dominated by the line-of-sight (LOS) path and the first order reflections. Additionally, propagation due to diffraction is not significant and therefore not practically viable as described later in this section. Compared to the more traditional RF frequencies, EHF (Extremely High Frequency) band (30 to 300 GHz) is much more sensitive to its propagation environment. From telecommunication point of view, the previously underutilized RF band introduces new challenges. Due to the small wavelength, most objects block or distort the signal causing fading, shadowing and scattering. In fact, the wavelength at these frequencies is so small that even particles in the atmosphere affect the signal propagation.

According to Friis transmission equation, the received signal power can be calculated from the effective isotropic radiated power (EIRP) which is then divided by surface area of a sphere at distance R from the transmitter and multiplied by effective area

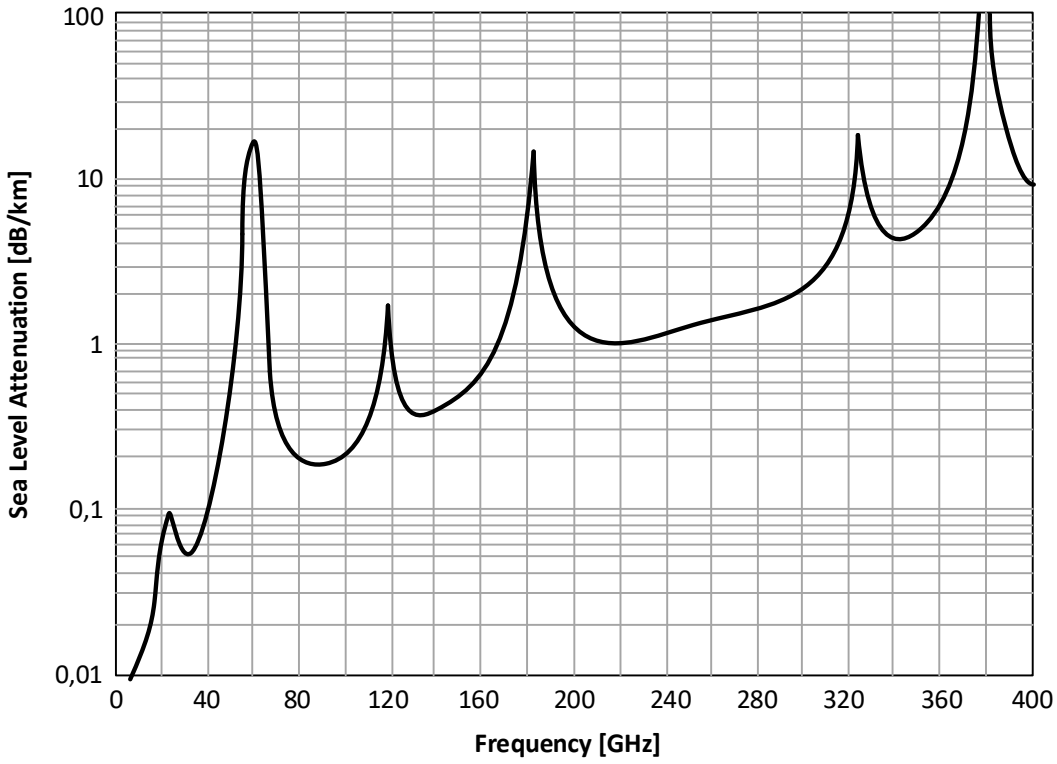

Figure 2.3 *Excess attenuation (dB/km) at sea level across sub-terahertz frequency bands. Adaptation of Fig. 2 in [15].*

of the antenna:

$$P_r = \frac{EIRP}{4\pi R^2} * A_{eff} = P_t G_t G_r \Big(\frac{\lambda}{4\pi R}\Big)^2 \tag{2.1}$$

where P_t is the transmitted power, λ is the wavelength of the signal, and G_t and G_r are the transmitting and receiving antenna gains respectively [25]. It can be seen that as the wavelength decreases, or frequency increases, the received power decreases relative to the square. To further elaborate this, let's assume two identical systems where one system operates at the traditional 5 GHz ISM band, for example IEEE 802.11a, and the other system operating at 60 GHz, e.g. IEEE 802.11ad. Now due to the higher operational frequency, the increased path loss translates to more than 20 dB. This is equal to tenfold increase in distance at 5 GHz.

Figure 2.3 illustrates the excess signal attenuation over the air as a function of

frequency at sea level. Note that this is an additional attenuation that comes on top of the previously discussed Friis distant dependent free space path loss. The attenuation peaks present in the Figure are caused by atmospheric effects, mainly due to signal absorption on water and air molecules. The density of these molecules therefore significantly impacts the excess attenuation. Consequently, low humidity and high altitude decrease the attenuation and vice versa. Furthermore, rain, hail, and snow drastically degrade the performance and need to be taken into account unlike in previous communication systems. Heavy rain can increase the path loss by 15 dB/km. According to measurements conducted previously, not only does rain attenuate the signal but it can also depolarize the signal. [13].

As was discussed in the previous section, IEEE 802.11ad operates at a frequency band from 57 GHz to 66 GHz, and it is not a coincidence that there is a large attenuation peak just at this frequency band. Usually these attenuation peaks, presented in Figure 2.3, would have been seen as a problem. On the contrary, new short range communication applications are designed to operate at precisely these frequencies. First of all, high attenuation equals low interference, and increased frequency reuse. For small networks, such as home networks, these characteristics are highly desirable. Additionally small coverage can be seen as a benefit since it makes eavesdropping harder. Admittedly, a growing number of consumers are more concerned about their privacy and security which might be a good selling point for millimeter wave applications. Furthermore, millimeter waves were initially (and still are) researched for military applications because of these previously mentioned characteristics [26].

In communications engineering, diffraction has been seen as a powerful propagation mechanism for non-line-of-sight (NLOS) communication scenarios. For example, when the terminal device moves behind a corner the signal can still reach it due to this phenomena. The idea is that when a signal encounters an obstacle, comparable in size to its wavelength, it creates a new point-like source of radiation, thus, enabling the signal to reach areas behind the object. However, at frequencies of hundreds of gigahertz the diffraction becomes highly unreliable as the attenuation can increase from 20 to 40 dB. [27]. Metal and wood edge diffraction at 60 GHz is presented in Figure 2.4. The presented diffraction losses are calculated from the unobstructed received power at incident angle $\alpha = 0$. Here HH and VV stand for horizontal and vertical transmit and receive polarizations respectively. As can be seen, in the shadow regions ($\alpha < 0$) the attenuation steeply increases with the angle.

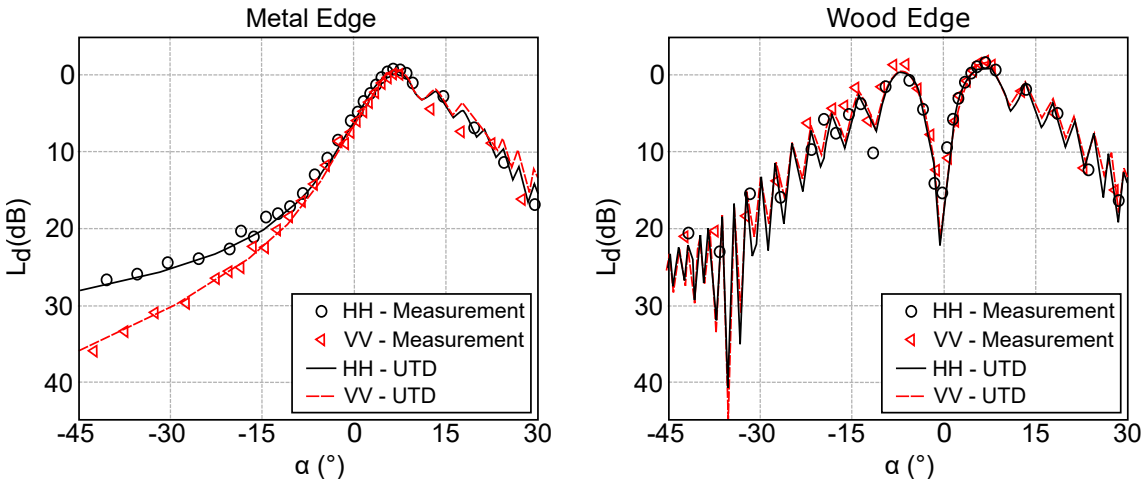

Figure 2.4 *Angular dependent diffraction loss at 60 GHz from a metal and a wood edge [27].*

In fact, a relatively small angle of 15 degrees equals an additional attenuation of 20 dB for the metal edge in comparison to the LOS path. In the lit region ($\alpha > 0$), the oscillations observed in the attenuation function are mainly due to interference between the LOS path and the diffracted field. Even though the lit regions for both of these materials are almost identical, the shadow region for the wood edge presents similar oscillating behavior as with the lit region. This is caused by interference between the diffracted field and the penetrated, or transmitted, field. Obviously this behavior is not seen with the metal edge. These results show that diffraction is not a reliable propagation mechanism for millimeter wave communication. Rather, millimeter wave communication systems need to rely on reflections, scattering and beam-steering techniques to overcome NLOS situations.

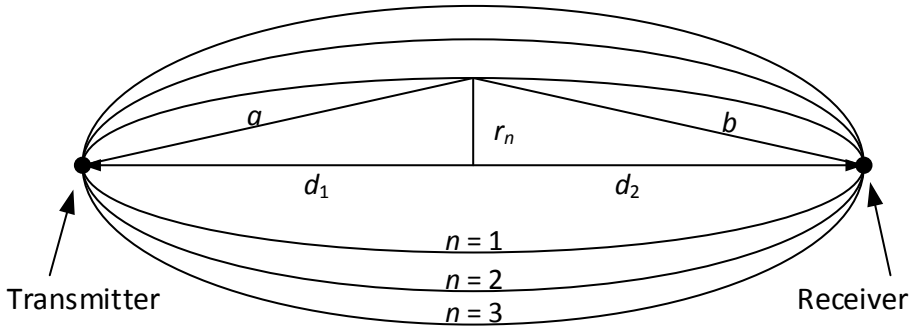

Figure 2.5 *Fresnel zones.*

Additionally, diffraction can also occur in cases in which the LOS path is not obstructed. The so called Fresnel zones are concentric ellipsoids around the LOS path which can be thought of as containing the main propagating signal energy as illustrated in Figure 2.5 [28]. In general, if the volume of the first ellipsoid is obstructed, the signal will be heavily attenuated. Especially at millimeter waves, the importance of the following Fresnel zones is negligible due to small wavelengths [13]. The ellipsoid of the nth Fresnel zone is defined by the locus point in which the distance $(a + b)$ is larger than the length of the LOS path $(d_1 + d_2)$ by n half-wavelengths. A common approximation for the radius r_n of the nth Fresnel zone is given by [28]:

$$r_n = \sqrt{\frac{n\lambda d_1 d_2}{d_1 + d_2}} \tag{2.2}$$

In contrast to diffraction, many materials seem to have very good reflective properties for millimeter waves. This is especially critical in indoor environments, such as, office areas which have lots of obstacles obstructing the potential LOS paths. Pioneering millimeter wave measurements conducted in the 90's show that many materials are highly reflective. In contrast to diffraction, losses caused by the signal reflection are in many cases less than 10 dB. A summarization of these results is provided in Table 2.1. The angle in the table indicates the angle of incidence. [29].

Table 2.1 *Reflection losses of various materials at 60 GHz [29].*

Material (thickness [cm]; estimated roughness [mm])	**Loss [dB] (10°)**	**Loss [dB] (20°)**	**Loss [dB] (30°)**	**Loss [dB] (40°)**	**Loss [dB] (50°)**	**Loss [dB] (60°)**	**Loss [dB] (70°)**
Granite (3; 0.6)	17.5	17.9	13.8	11.7	7.9	5.5	3.4
Quartzite (2; 0)	5.8	3.4	3.1	24.1	2.1	2.1	4.4
Marble (1.7; 0)	3.8	2.7	2.7	5.5	5.8	2.1	0.8
Limestone (3; 0)	6.5	5.8	5.5	5.1	4.1	3.1	1.9
Concrete (5; 0.1)	7.5	7.2	6.7	6.2	5.3	4.1	2.0
Brick (11; 2)	14.8	12.7	13.4	17.5	12.3	8.6	4.8
Tiles (0.5; 0.1)	4.1	3.8	4.1	3.8	5.8	7.6	2.1
Glass, rough (0.4, 0.3)	6.7	6.2	5.2	3.8	2.9	2.2	0.8
Glass, smooth (0.4, 0)	17.6	14.6	10.8	7.6	5.3	3.8	2.9
Glass, smooth (0.2, 0)	11.4	9.8	8.3	6.7	4.8	3.4	2.7
Plasterboard (1.4; 0)	14.1	14.1	8.3	5.5	9.8	5.1	1.2
Plasterboard, rough (1; 1.7)	≥ 30.0	≥ 30.0	≥ 30.0	≥ 30.0	≥ 30.0	≥ 30.0	16.9

The Table shows that the reflection losses caused by the most typical materials found in an office environment are relatively minor. Interestingly, rough glass seems to reflect more than a smooth glass. This is most likely due to the fact that more of the signal is refracted to the smooth glass than to the rough one. On the other hand, loss is greater from a rough plasterboard than from a smooth one, because the signal is strongly scattered from the much rougher surface.

Table 2.2 *Penetration losses of various materials at 60 GHz [29].*

Material (thickness [cm]; estimated roughness [mm])	Granite (3; 0.6)	Quartzite (2; 0)	Marble (1.7; 0)	Limestone (3; 0)	Concrete (5; 0.1)	Brick (11; 2)	Tiles (0.5; 0.1)	Glass, rough (0.4, 0.3)	Glass, smooth (0.4, 0)	Glass, smooth (0.2, 0)	Plasterboard (1.4; 0)	Plasterboard, rough (1; 1.7)
Penetration Loss [dB]	≥ 30.0	3.4	5.2	≥ 30.0	≥ 30.0	16.9	≥ 30.0	4.5	2.4	1.7	2.8	≥ 30.0

Penetration losses for the same materials are presented in Table 2.2. It can be seen immediately that millimeter waves have very poor penetration properties, as was to be expected. Examining both characteristics of these materials, one can see that some materials have very high penetration losses and low reflection losses, for example, limestone, whereas, some materials perform poorly on both metrics, namely, the rough plasterboard. It is intuitive to think that thick and dense materials with a smooth surface perform better as reflective surfaces and vice versa. It is good to note that, even though glass performed well in both metrics, transparency has a significant impact into its reflection and penetration properties as was shown in [30].

While scattering has not been seen as an important propagation mechanism in today's cellular and WLAN systems, it becomes a powerful mechanism at millimeter waves due to the fact that most objects, such as lampposts, humans, foliage and cars, are much larger than the wavelength of the signal. Paths created by a scatterer might be even stronger than the reflected paths [13]. One popular method for estimating scattering from different physical objects is to use radar cross section (RCS). The RCS represents how the intercepted electromagnetic waves are scattered from the object. It is important to note that the RCS does not strictly depend upon the physical size of the object, for example, a large RCS does not necessarily mean

that the object is physically large. Hence, the most important characteristics of an object, when it comes to scattering, are the object's roughness and its RCS. Typically the RCS formulas are represented for scenarios where transmitter and receiver occupy the same point in space (namely radars). However, this monostatic cross section is not well suitable for communication systems where the system is designed for transmitting information from one point to another. For the so called bistatic scenarios, the RCS is defined as:

$$\sigma_{3D} = \lim_{R\to\infty}\left(\frac{4\pi R^2 S_s}{S_i}\right) = \lim_{R\to\infty}\left(\frac{4\pi R^2 |E_s|^2}{|E_i|^2}\right) \tag{2.3}$$

where R is the distance between the receiver and the scatterer, S_s is the scattered power density towards the receiver, S_i is the incident power density, and E_s and E_i are the scattered and incident electric fields respectively. Particularly, the received power can be easily estimated from the RCS by multiplying it with the scattered field. [13].

When it comes to WLAN and WPAN systems, indoor propagation aspects are understandably more interesting than outdoor aspects. As was mentioned earlier, the millimeter wave propagation is often described to be quasi-optical, where the LOS and first order reflection paths are the most dominant paths to the receiver. Furthermore, as was mentioned, millimeter waves are more sensitive to their environment as even small objects tend to be large in comparison to their wavelength. This causes the signal to interact more with its surroundings causing increased losses, signal polarization and so on. While millimeter waves have relatively high penetration losses, reflection losses are not that substantial, as was shown. Especially in an indoor environment, where the amount of obstacles increases drastically, the LOS path is more often than not obstructed. Therefore, the reflective properties of various materials become increasingly interesting. From an implementation point of view, beamforming, which will be discussed in the following section, becomes much more important as the NLOS paths may fluctuate or be blocked completely as the reflective paths change or the orientation of the terminal devices change.

2.3 Multi-Gigabit RF and Baseband Circuits

Major building blocks of any RF system are the power amplifier (PA), mixer, low noise amplifier (LNA), and voltage controlled oscillator (VCO). Systems having

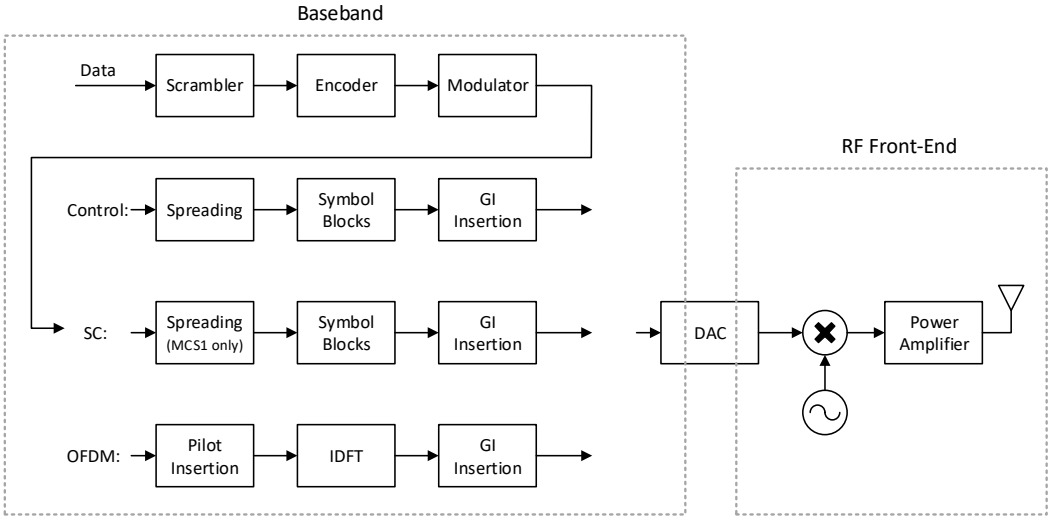

Figure 2.6 *Simplified IEEE 802.11ad transmitter block diagram (adaptation of Fig. 10 in [31]). It should be noted that same modulation and coding schemes are not explicitly shared by the different physical layers.*

strict spectral mask requirements or using complex modulation typically include a phase-locked loop (PLL) with the VCO. This subchapter briefly addresses the challenges introduced to these blocks when operating at millimeter wavelengths.

These building blocks are presented in Figure 2.6 which illustrates a generic IEEE 802.11ad transmitter block diagram. In the receiver side, the PA is replaced by a LNA and the digital-to-analog converter (DAC) with an analog-to-digital converter (ADC). The baseband blocks are not that relevant in this context, and will be discussed in the next chapter.

When designing a communication system, a good starting point is to consider the sensitivity, link budget and receiver noise requirements. For a communication system to operate properly, the radio must satisfy the signal-to-noise ratio (SNR) requirements of the modulation scheme used. While the SNR can be considered as a baseband design requirement, link budget helps understand how these requirements can be achieved. Link budget can be derived from the Friis transmission equation (2.1) by expressing it in logarithmic scale:

$$P_r = 10\log_{10}\left(P_t G_t G_r \left(\frac{\lambda}{4\pi R}\right)^2\right) = P_t + G_t + G_r + 20\log_{10}\left(\frac{\lambda}{4\pi R}\right) \tag{2.4}$$

Note that even though same symbols are used for powers and gains, these values are in decibel scale. In literature the last term, usually denoted as L_d or simply L, is called the free space path loss. Next step is to determine the thermal noise power of the system:

$$P_{noise} = 10\log_{10}(kTBF) = 10\log_{10}(kT) + 10\log_{10}(B) + 10\log_{10}(F) \tag{2.5}$$

where k is the Boltzmann constant, T is the receiver temperature in Kelvins, B is the system bandwidth, and F is the noise factor of the receiver [25]. It should be noted that sometimes in the literature noise figure and noise factor are used as synonyms. This is partly true, but usually noise factor is presented in linear values and noise figure as decibels. Thus, the relation is $NF = 10\log_{10}(F)$. Additionally, the noise factor for a receiver can also be calculated with Friis formula if the individual noise factor F_n and power gain G_n values are known for the components in the receiver chain [25]:

$$F_{tot} = F_1 + \frac{F_2 - 1}{G_1} + \frac{F_3 - 1}{G_1 G_2} + \frac{F_4 - 1}{G_1 G_2 G_3} + ... + \frac{F_n - 1}{G_1 G_2 ... G_n} \tag{2.6}$$

It should be emphasized that these noise factor and gain values are in linear scale. Notice also how the first components in the receiver chain, starting from the antenna, have much larger impact to the total noise factor as the latter components are divided by the cumulative gain of the receiver chain.

Let us consider an example, where a system operating at 60 GHz is transmitting over a one meter link. Assuming 10 dBm transmit power and unity gain antennas, the received power is:

$$P_r = 10 \text{ dBm} + 0 + 0 + 20\log_{10}\left(\frac{\frac{3*10^8}{60*10^9} \text{ m}}{4\pi * 1 \text{ m}}\right) = 10 \text{ dBm} - 68 \text{ dB} = -58 \text{ dBm}$$

Further assuming bandwidth of 2.16 GHz, operating temperature of 323.15 K, and a typical noise figure of 5 dB, the receiver noise power becomes:

$$\begin{aligned} P_{noise} &= 10\log_{10}(1.381 * 10^{-23} * 323.15)\frac{\text{dBW}}{\text{Hz}} + 10\log_{10}(2.16 * 10^9 \text{ Hz}) + 5 \text{ dB} \\ &= -104 \text{ dBW} \cong -74 \text{ dBm} \end{aligned}$$

Thus, the SNR for this example is -58 dBm $-(-74$ dBm $) = 16$ dB. If the calculated SNR exceeds the SNR requirement, that remainder is called link margin. However, this type of analysis does not take into account the implementation losses that are in place for practical systems nor is the propagation loss estimation as straight forward as this model suggests. Yet, it is a good starting point when designing a system. This analysis already shows us some key things considering millimeter wave systems. First, the received power sharply decreases if the distance is increased. For example, at ten meters the power decreases by 20 dB. Second, due to the extremely large bandwidth, the noise power is much higher compared to lower frequency legacy systems.

2.3.1 Analog Millimeter Wave Components

PA is usually the last transmitter chain component before the antenna. PAs are key to achieving the calculated link budget and are traditionally one of the most power consuming components of the device. Therefore, it is important to find a balance between adequate output power, sufficient linearity and power efficiency. To make things more complicated, certain modulation schemes, such as orthogonal frequency-division multiplexing (OFDM), require large dynamic ranges. OFDM is problematic due to high peak-to-average-power ratios (PAPR) where the input signal on average has low power but time to time contains high power peaks. If the PA input power is much lower than the desired output power, the gain of the PA is also something to consider. It has been shown that transistor power gain is proportional to $20 \log\left(\frac{f_T}{f}\right)$ where f_T is the transit frequency and f is the operational frequency. Clearly, higher operational frequency results into lower gain per transistor which has to be taken into account at 60 GHz in the PA design. [13]. One promising PA architecture is the Doherty design which consists of a main amplifier and a smaller auxiliary amplifier. At low input power levels the main amplifier operates alone near saturation with high efficiency. If the input power increases, the auxiliary amplifier contributes by providing additional power without compromising linearity and efficiency. [15]. Additional PA architectures that are applicable to millimeter waves are shown in [13–15].

Similarly to the PA at transmitter side, LNAs are used in the receiver. LNA is usually the first component after the antenna. This is due to the fact that as was discussed earlier, the first component in the receiver side has the largest impact to

the noise figure of the receiver. Therefore, the most important characteristics of a LNA are its noise figure and gain. Obviously, these requirements should be met with adequate linearity and dynamic range. At millimeter waves, these requirements become more difficult to achieve and usually stages are needed to achieve the desired gain [15].

Mixers are nonlinear circuits responsible for downconverting or upconverting a signal between RF and intermediate frequency (IF). In an active mixer the LO signal modulates the transconductance of the cascade transistor, whereas, in a passive mixer the LO modulates a switch. There are three criteria by which mixers are usually judged: conversion gain, linearity, and isolation. Active mixers provide conversion gain through amplifying transistors, while passive mixers use simple switches, resulting in a conversion loss. In addition to the linearity perception presented with amplifiers, nonlinear mixers also introduce new frequency components called harmonics which need to be taken into account in the system design. Isolation refers to the ability to shield the output signal from the input signals, for example, the IF output from the input RF and LO signals. Even though passive mixers are easier to implement and can achieve better linearity, they require higher LO power levels to switch robustly. The problem arises as high LO powers are difficult to achieve at 60 GHz due to the same transistor gain issue discussed earlier. [15]. Summaries of various millimeter wave mixer designs reported in the literature can be found in [14, 15].

The PLL, or frequency synthesizer, is one of the most important and challenging blocks of a millimeter wave radio. PLLs are so important because they are needed for producing the LO, channel selection and for producing low-jitter clock signals for gigabit per second data rate baseband. A basic PLL consists of a phase detector, a low pass filter, a VCO, and a frequency divider. Essentially, the PLL is a feedback loop that detects the phase difference of its input and output and then tries to equalize the phase difference by controlling the VCO. Keeping the input and output phases in lock also implies keeping the frequencies the same. By controlling the frequency divider, the VCO can be tuned across the whole frequency band that is used by the system. Usually, a much lower frequency signal is used in the frequency divider to provide low phase noise reference. Instead of VCOs, typically temperature compensated crystal oscillators are utilized to provide this reference signal as high accuracy and low phase noise are essential. If the fundamental frequency of the VCO is much lower than the RF frequency, multipliers are required. However, not

only do these multipliers reduce the LO power level, but also increase the phase noise. [13]. Compilation of different VCO architectures reported in the literature is provided in [14].

2.3.2 Multi-Gigabit Baseband

ADC connects the analog and digital portions of the circuitry together, as they convert the continuous analog signals into discrete digital signals. The analog input signal is quantized by sampling it periodically. The dynamic range, or the effective number of bits per sample, ultimately determines the resolution of this conversion. Consequently, the resolution determines the quantization error, in other words, the difference between the actual analog values and the discrete quantized values. The Nyquist-Shannon theorem states that, if the sampling rate is greater than twice the bandwidth of the signal being sampled, the signal can be perfectly reconstructed assuming ideal ADC and neglecting the quantization error.

A fundamental challenge in ADC designs is the power-bandwidth product, which requires the designer to trade-off between sampling rate and resolution. Regardless of the application, designer's goal is to adequately sample the signal while not consuming unnecessary amount of power. [15]. This challenge is further amplified at millimeter waves since much larger bandwidths are in use. Clock jitter is the deviation of a presumed periodic signal, which causes timing mismatches in sampling, resulting in erroneous conversion. Since jitter is proportional to the slew rate of the desired signal, the error increases as the frequency of the signal increases. Thus, clock jitter becomes a challenge in very high speed converters that are required for millimeter wave systems. At the time of writing this thesis, the research around high-speed ADCs with wide bandwidths is vivid and numerous different approaches have been presented in various research articles. A very potential architectural example is the flash ADC which offers very high sampling rates but suffers from low achievable resolution [14, 15].

2.3.3 Millimeter Wave Antennas

At frequencies below 10 GHz, antennas have been their own component in the system design, usually connected with coaxial cables, due to the relatively large wavelengths used. On the contrary, at millimeter wavelengths the antenna size

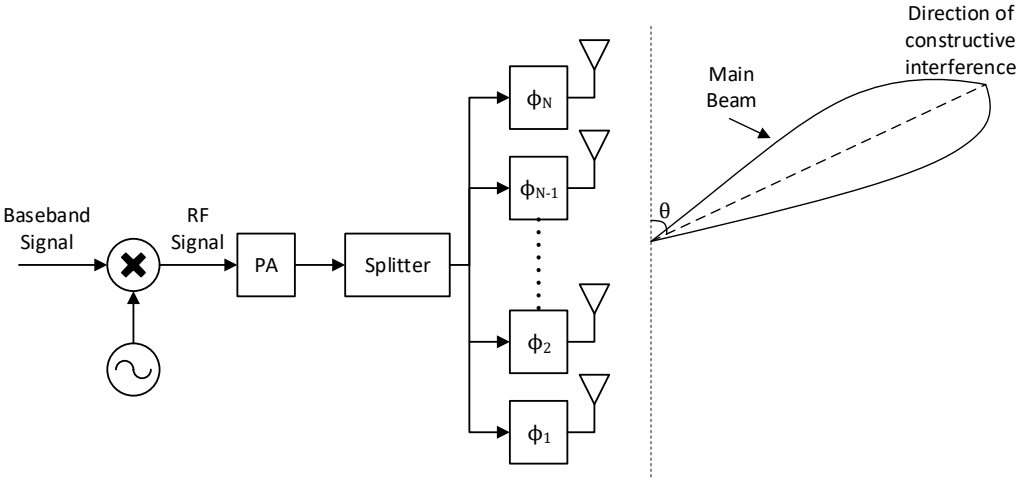

Figure 2.7 *An offset phase front generates constructive interference resulting into a steerable antenna beam.*

can be drastically reduced. The miniaturization of antennas at these frequencies allows the implementation of antenna arrays which is a key advantage. An antenna array consists of periodically arranged antennas in either one- or two-dimensional configuration. Phase difference between the elements then determines the direction of the antenna array beam as the differently phased signal components sum up constructively or destructively.

In physics, this phenomenon is explained by the principle of superposition of waves. The principle states that when two waves are incident on the same point, the amplitude of the resultant wave at that point is equal to the vector sum of the individual waves. Constructive interference occurs when the phase difference of the waves is multiple of 2π rad , whereas, destructive interference occurs when the difference is odd multiple of π rad. [32].

Figure 2.7 illustrates how an antenna array works. The amplified RF signal is fed to all N antenna elements, where every element has its own phase shift. These phase shifts can be controlled individually and thus the main beam can be arbitrarily steered to different directions. A widely used approximation for calculating these individual phase shifts is given as:

$$\phi_n = -(n-1)k_0 d\cos\theta, \qquad 0 \leq n \leq N \tag{2.7}$$

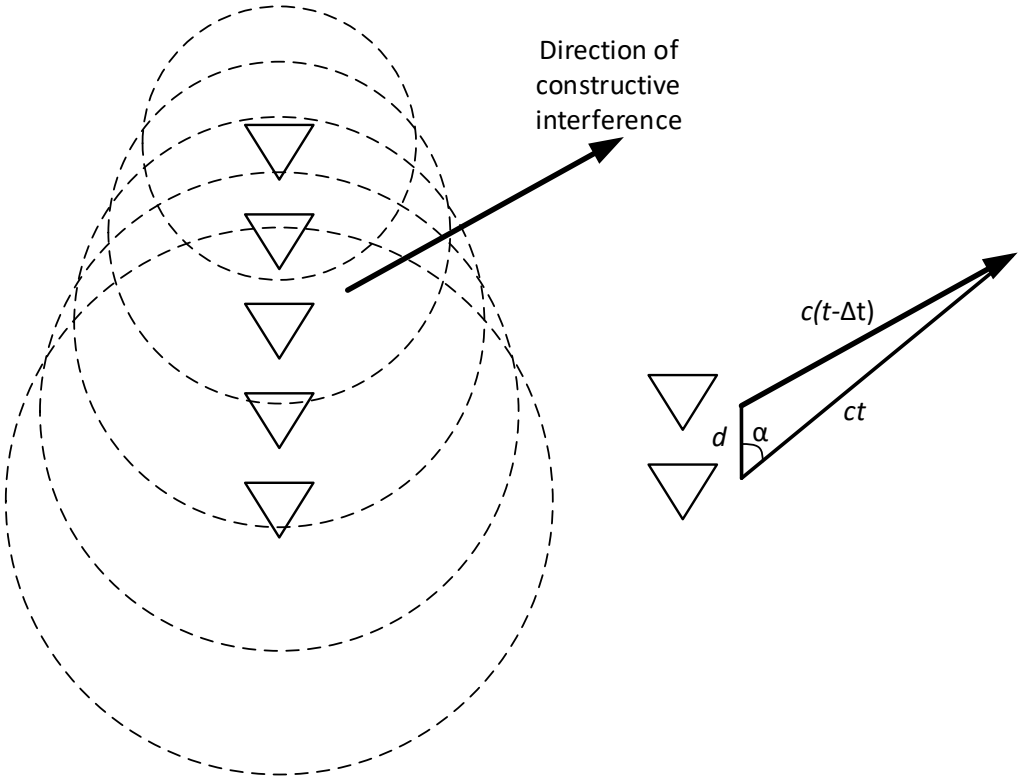

Figure 2.8 *Differently phased isotropic antenna elements excite phase fronts that add constructively at angle α. [13]*

where n is the antenna element index, k_0 is the wavenumber, and d is the distance between elements [13].

To elaborate this, consider an example shown in Figure 2.8, where each element of the antenna array creates a phase front propagating outwards from its respective antenna. The triangle on the right geometrically illustrates how the different phase fronts constructively sum up at angle α, being the beam direction. With law of cosines we can write:

$$(ct - c\Delta t)^2 = d^2 + (ct)^2 - 2dct\cos\alpha \tag{2.8}$$

where c is the speed of light. Solving this equation for $\cos\alpha$ we get:

$$\cos\alpha = \frac{\left(\frac{d}{c}\right)^2 - \Delta t^2 + 2t\Delta t}{2t\left(\frac{d}{c}\right)} \tag{2.9}$$

Substituting $\Delta t = \left(\frac{d}{c}\right)\cos\theta$ leaves us with:

$$\cos\alpha = \left(\frac{d}{2ct}\right)\sin^2\theta + \cos\theta \tag{2.10}$$

Now, as ct is a large value, relative to the other values, it will result the first term to be negligible. Thus, we will see that $\cos\alpha \cong \cos\theta$. Therefore, the excitation time difference Δt corresponds to a phase difference of $2\pi f\Delta t = 2\pi f\left(\frac{d}{c}\right)\cos\theta = k_0 d\cos\theta$, which proves that the phase shift approximation in Equation 2.7 does result into a beam pointing at the direction θ as was represented in Fig. 2.7. [13].

The maximum angle of beam steering θ_{max} is determined by the spacing between elements. At angles larger than the θ_{max}, grating lobes start to degrade the antenna performance. Grating lobes are large side lobes of the antenna pattern that lower the directivity and gain of the antenna array. These grating lobes may have destructive consequences to the overall performance of the system, as highly directional communication relies on unambiguous detection of the received signal direction. Therefore, the spacing between elements d has to be below [13]:

$$d \leq \frac{\lambda}{1 + \cos\theta_{max}} \tag{2.11}$$

The definition of the steering angle needs to be emphasized here (see Fig 2.7). It is the angle between the beam and the line that is *parallel* with the array. However, often in literature and industry, the stated steering angle is actually the angle between the beam and the line that is *perpendicular* to the array. We shall use the latter definition from now on.

Antenna arrays have a long history and first implementations saw operational action in the World War II [14]. However, these structures have been enormous as the frequencies used were much lower. At millimeter waves these type of antennas are

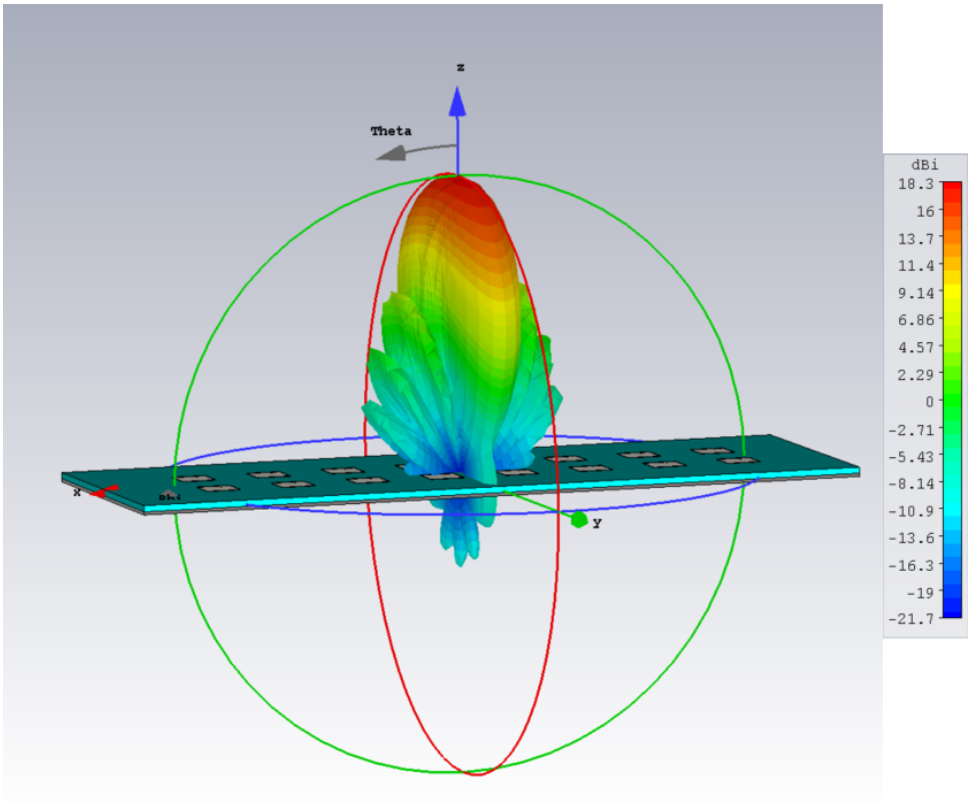

Figure 2.9 *Simulated directivity of a 2x8 phased antenna array of patch antenna elements when the array is not steered.*

small enough to be integrated into mobile devices. As an example, model and directivity of a 16-element phased antenna array operating at 60 GHz is presented in Figure 2.9. The array consists of patch antenna elements that are arranged in a 2x8 configuration.

To further elaborate the size benefits, at 60 GHz a quarter wave dipole is only 625 μm long assuming relative permittivity of 4. Consequently, a 100-element antenna array arranged in a square pattern would only require $100 * 625\,\mu\text{m} * \sqrt{2} = 8.82$ mm in both dimensions. To give it some perspective, that is 24 times less than it would be at 2.4 GHz. [13]. Due to the extremely small size of these millimeter antennas it is now possible to integrate the antenna to the integrated circuit (IC) and not have it as a separate component. This reduces costs as the antenna can be done in the same circuit fabrication process, and also makes previously used antenna connectors and coaxial cables obsolete. There are basically two different approaches: either the antenna is fabricated in the packaging technology used to

house the RF module or the antenna is integrated in the printable circuit board (PCB) housing the transceiver. Both of these options have the benefit of cutting costs and reducing implementation losses. On the other hand, highly integrated millimeter wave antenna arrays usually struggle to obtain even average radiation efficiencies. The antenna efficiency indicates the amount of power that is radiated in contrast to the overall input power, rest of the input power is assumed to be losses. Especially simple millimeter wave on-chip antennas may only achieve efficiencies of 10 %, whereas, in-package antennas may achieve efficiencies of 80 %. With exotic materials and lenses the efficiency of on-chip antennas can be increased to roughly the same level. [13].

High antenna gain in small physical size is the enabling characteristic at millimeter wave systems. These high gains are achieved by using tight beamwidths that are made possible by these electrically large antenna arrays. Electrically large refers in this context to the size of the antenna array in comparison to the signal wavelength. The maximum antenna gain of a linear antenna array of N elements is proportional to:

$$G_{max} \propto \frac{4\pi e_{max}(ND_{element})^2}{\lambda^2} \tag{2.12}$$

where e_{max} is the maximum efficiency of the antenna array (always ≤ 1), and $D_{element}$ is the maximum length of a single antenna element. If the antenna array is a two-dimensional array with N^2 elements, the formula still holds but the effective area and therefore the gain increases even more due to increased number of elements. [13]. The formula shows that the gain increases to the square of the size of the array. Thus, the gain of the array can be relatively easily increased by just increasing the number of elements in the array. Additionally, gain increases to the square when the wavelength is decreased, which is obviously beneficial at millimeter wavelengths. For these reasons, it has been predicted that future millimeter wave systems will include hundreds of antenna elements.

Beamwidth of an antenna array decreases linearly with the increase in size of the antenna array, with a good rule of thumb [13] as:

$$Beamwidth \approx \frac{60^\circ}{\left[D/\lambda\right]} \tag{2.13}$$

where D is the length of the antenna array in the plane of which the beamwidth is being calculated. It should be noted that in the above formula, the dividend angle

slightly varies depending on the reference.

The tight beamwidth is also good at reducing interference which has been a problem especially with legacy WLAN systems. However, this does not come without drawbacks as tight beams require more complex transceivers that support beam steering and beamforming algorithms. These implementation challenges will be discussed in more detail in the following chapter.

The phase offsets in the antenna array, shown in Fig. 2.8, may be accomplished in many ways. Analog approaches include RF phase shifting, IF/baseband phase shifting, and LO phase shifting. In practice, these can be implemented by using delay lines or by slightly adjusting the LO frequencies with a VCO/PLL. Digital approaches use various buffer lengths to perform the phase shift. The RF phase shifting requires less die space as the combiner/splitter can be implemented before the mixer, which also relaxes linearity requirements for the mixer as signals outside the main beam will be cancelled. However, RF phase shifters are hard to implement at millimeter wave frequencies. Similarly, IF/baseband phase shifting relies on analog phase shifters, which are easier to realize at lower IF/baseband frequencies. On the other hand, this increases linearity requirements for the mixer in the receiver as it has to sustain undesired signals. LO phase shifting has the advantage of removing the phase shifter out of the signal path. Additionally, the analog phase shifter can be narrow band which makes it easier and cheaper to implement. A disadvantage of this approach is that the phase shifter will reduce the LO power arriving to the mixer unless an amplifier is used. Ultimately the beam steering approach determines what kind of phase shifting will be implemented and whether discrete or continuous phase shifting is required. [13].

Beam steering can be implemented in two different ways, either with switched-beam approach or with adaptive approach. The switched-beam approach, also known as code-book approach, introduces finite number of possible preconfigured radiation patterns. An example of this approach is shown in Figure 2.10. It should be noted that the patterns are presented in azimuth plane. First, the quasi-omni patterns are used to locate devices in the proximity and also to determine the rough direction of those devices. Next, during the hand shake or negotiation phase, sector patterns are utilized to further define the direction of the target device. Finally, communication link is established and beam patterns are used to transmit and receive information. Further tracking and refinement of beam patterns can be carried out afterwards.

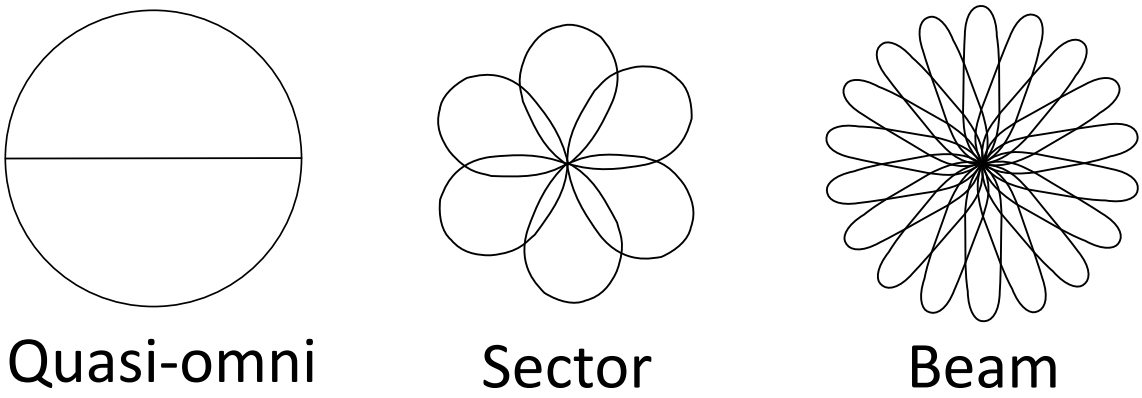

Figure 2.10 *Beam steering switched-beam approach with three levels of antenna patterns [13].*

Adaptive schemes take a very different approach as they use complex algorithms to dynamically adjust the radiation pattern and theoretically have infinite number of possible radiation patterns. Obviously, the benefit of switched-beam approach over the adaptive approach is reduced complexity, which is desirable in low cost and low power devices. However, this compromises the optimal performance as the finite number of patterns may not contain an optimal pattern for every situation. Especially with moving users, the adaptive approach can smoothly track the user, whereas, in the switched-beam approach the pattern needs to be continuously changed which causes the received signal strength to fluctuate. On the other hand, this can be to some degree be mitigated by increasing the discrete phase set which then of course increases the complexity. [33].

3. IEEE802.11AD: DIRECTIONAL MULTI-GIGABIT WLAN AT 60 GHz

Compared to the past IEEE 802.11 standards, or amendments, the IEEE 802.11ad takes a drastic new approach by operating at 60 GHz frequency band. As mentioned in the chapter 2, close to ten gigahertz of spectrum is allocated globally for this use. Therefore, unlike the previous amendments, IEEE 802.11ad focuses less on increasing the spectrum efficiency as extremely large bandwidths alone enable gigabit per second throughputs.

Table 3.1 *Common device types utilizing IEEE 802.11ad [34].*

Device	Antenna sectors	Expected range (m)	Maximum throughput (Gbps)	Traffic type	Antenna arrays
AP, Dock	32 to 64	20	7	Bursty on DL	≤ 3
Display, TV	32 to 64	5 to 10	7	Continuous (mainly DL)	≤ 2
Laptop	16 to 32	5 to 10	4.6 to 7	Various (symmetric UL & DL)	≤ 2
Tablet	2 to 16	2 to 5	4.6	Various (symmetric UL & DL)	1
Handheld	≤ 4	1 to 5	1.2 to 4.6	Various (symmetric UL & DL)	1
Wireless peripheral	≤ 4	0.5 to 2	1.2 to 4.6	Bursty	1

Table 3.1 illustrates some of the more common device classes to be found using

IEEE 802.11ad. In the table, DL and UL stand for downlink and uplink, respectively. From the table we can see the wide variety of different kinds of devices and communication needs. Therefore, communication at millimetre waves is ideal for this purpose as it allows high spatial reuse due to low interference and offers extremely high throughputs.

One of the most advertised use cases of the IEEE 802.11ad is the wireless video streaming [24, 31, 35, 36]. Even thought wireless video streaming has been possible with the legacy IEEE 802.11 standards[1], it has not really been feasible since heavy compression is needed. Problem with compression is that it is computationally heavy, may cause visual artifacts, and usually introduces some latency. Latency is especially problematic if the user is interacting with the device. In comparison, the IEEE 802.11ad offers enough capacity to support visually lossless streaming of the device display output, even at high resolutions. Additionally, low latencies make it possible to use human interface devices, such as, a keyboard and a mouse if they are connected to a dock or an external display. Obviously, the sheer amount of completely different use cases requires a reconsideration of the network structure. Hence, the previously heavily centralized network structure of the IEEE 802.11 standard is enhanced to better satisfy this peer-to-peer type of a communication scheme [4].

3.1 Overview

Spectrum regulation at 60 GHz was already addressed in the previous chapter. As a short recap, IEEE 802.11ad uses frequency band of $57 - 66$ GHz, which is further divided into four channels, each with bandwidth of 2.16 GHz. The channel 2 was chosen as the default channel, as it is available worldwide. The spectrum allocation was illustrated in Figure 2.1 and a transmit mask was presented in Figure 2.2. A simplified transmitter block diagram was shown in Figure 2.6, the baseband portion will be further discussed in this Chapter.

IEEE 802.11ad uses highly directional and steerable transmission beams to mitigate interference, increase spatial reuse, and increase throughput. These antenna implementations were discussed in the Section 2.3.3. It should be noted that even though highly directional transmissions are used in IEEE 802.11ad, the standard does not

[1] Mainly with Miracast [37]

support multiple input multiple output (MIMO) schemes which have become increasingly popular in other wireless communication systems. This is due to the fact that, for many lower frequency band systems the only way to increase capacity is to increase spatial (or spectral) efficiency. In comparison, the 2 GHz wide channels of IEEE 802.11ad alone offer enough capacity to achieve gigabit per second data rates.

However, directional transmissions do not come without drawbacks. Performance of the system relies heavily on beamforming, thus, poorly trained beams can cause severe performance loss. This problem arises especially in NLOS communication where it might be difficult to determine the best available path to the receiver. Another fundamental issue in directional transmissions is deafness. Traditional WLAN systems have been designed around an idea that all stations (STA) are able to hear on-going transmissions and a STA defers its own transmission if the medium is sensed to be in use. This method works well with omnidirectional transmissions that are used in legacy WLAN systems but for IEEE 802.11ad, the MAC has to be redefined. Consequently, this will be discussed later in this chapter.

3.2 MAC Layer

Distributed coordination function (DCF) with classic carrier sense multiple access with collision avoidance (CSMA/CA) introduced in the legacy IEEE 802.11 standard cannot adequately service the directional multi-gigabit (DMG) PHY. The fundamental idea behind DCF is to listen to the medium and defer the appending transmission if the medium is found to be in use by another user. Due to the highly directional links and higher path losses, device discovery becomes much more difficult and this method, previously relying on omnidirectional transmissions, does not work as intended. Hence, the IEEE 802.11ad amendment introduces a concept of personal basic service set (PBSS) which allows the stations to communicate in an ad-hoc manner [4]. Additionally, use cases, such as, wireless display or storage use, require ad-hoc approach due to the fact that usually no pre-installed infrastructure exists. In PBSS the DMG access is granted by a personal service set control point (PCP) or by an access point (AP). In an ad-hoc network, the PCP is chosen among the stations so that the PCP has the most complete set of IEEE 802.11ad capabilities and services for the network [4]. This procedure is also used in PCP handover which addresses the fundamental problem where the whole PBSS network paralyzes if the PCP is lost.

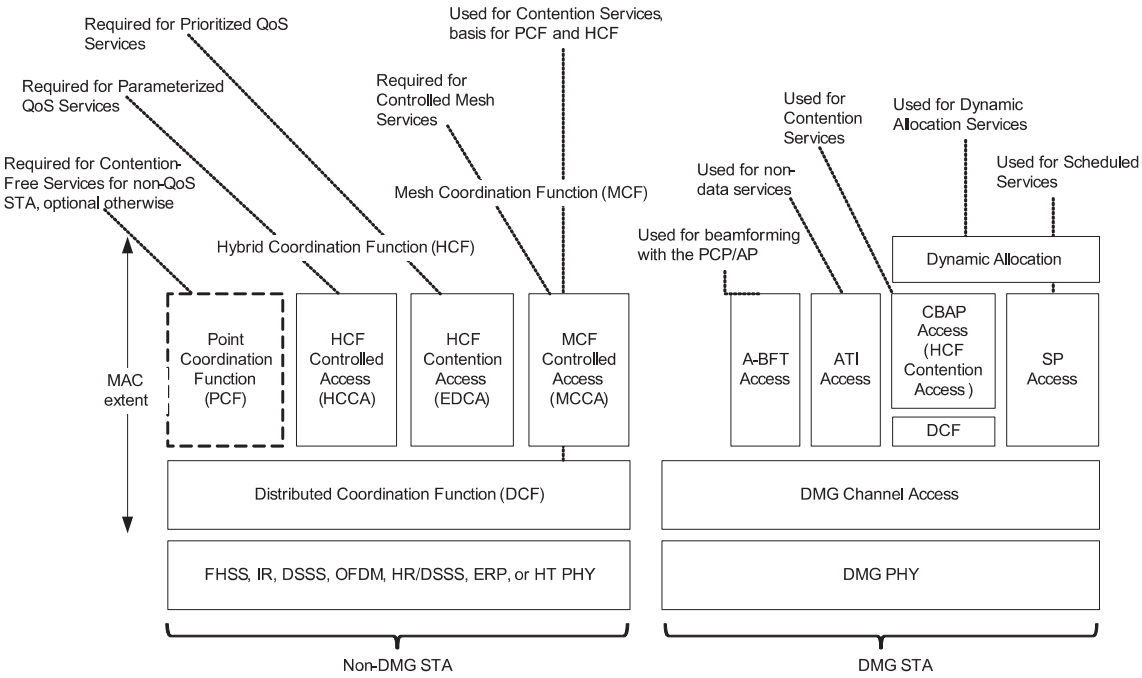

Figure 3.1 *MAC architecture comparison between legacy non-DMG STA and DMG STA [4].*

As can be seen from Figure 3.1 the largest difference in MAC architecture is the introduction of DMG channel access to replace the legacy DCF. Nonetheless, DCF is still available for DMG STAs during contention-based access periods (CBAP) but it has been enhanced to suit the constraints of DMG PHY. For example, due to the hidden node problem in directional links, the transmission is advised to be pointed at the intended receiver (direction must be known prior to transmitting). In contrast to the previous WLAN amendments, the IEEE 802.11ad takes a hybrid MAC approach to satisfy the various use cases envisioned for it. Therefore, it supports contention-based access, scheduled channel time allocation and dynamic channel time allocation. The latter two being based on a time-division multiple access (TDMA) and a polling mechanism. [34]. These methods will be discussed in detail later on this chapter, and an in-depth comparative evaluation of these MAC methods can be found from [38].

In lower frequency bands, namely 2.4 GHz and 5 GHz, the IEEE 802.11 medium access happens through periodic beacon intervals (BI) that are transmitted omnidirectionally by the AP in a beacon frame. Purpose of this beacon is to announce the existence of a WLAN network. The remainder of the BI can be used for data trans-

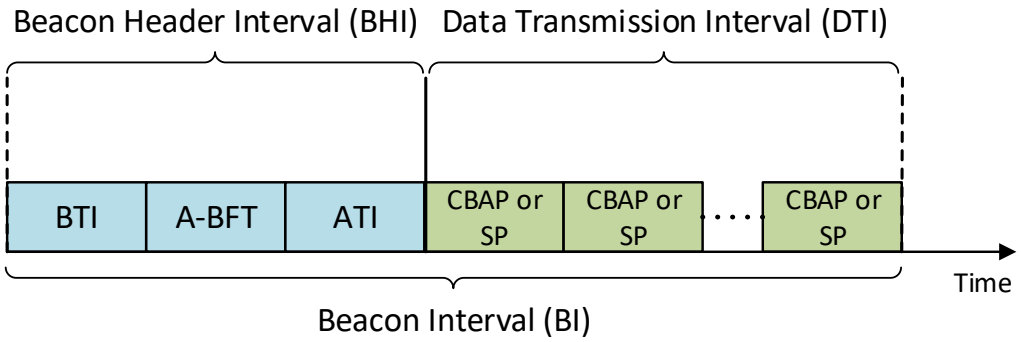

Figure 3.2 *IEEE 802.11ad beacon interval structure.*

mission between stations, followed by a contention-based access scheme. Length of the BI is limited to 1000 ms, however, typically chosen around few hundred milliseconds. Reason behind this is the fact that, while longer interval reduces the management overhead and therefore increases throughput, it also increases delays and latencies. [39].

This beacon concept is further redefined by the IEEE 802.11ad amendment for it to cope with the challenges introduced in the millimeter wave propagation. Figure 3.2 illustrates an example beacon interval structure. The BI consists of a beacon header interval (BHI) and a data transmission interval (DTI). Those are further divided into:

- *Beacon transmission interval (BTI)* – Used by a PCP to announce the network. The BTI consists of multiple beacon frames, each transmitted from a different antenna sector so that all directions are covered with decent range. It is not mandatory for all BIs to contain a BTI. A STA that is not a PCP should not transmit during a BTI of the PBSS of which it is a member of.

- *Association beamforming training (A-BFT)* – Beamforming training period reserved for STAs to train their antenna system configuration for communicating with the PCP that transmitted the BTI. Likewise, not mandatory for all BIs.

- *Announcement transmission interval (ATI)* – Reserved for PCPs to exchange management information with the participating and beamtrained STAs.

- *Scheduled service period (SP)* – Each SP is assigned to a STA-to-STA communication as a contention-free period by the PCP.
- *Contention-based access period (CBAP)* – Multiple STAs can compete for the channel access as defined by the enhanced distributed channel access (EDCA) rules. During a CBAP, STAs can request SP allocations.

The medium access during CBAP follows EDCA which is provided in hybrid coordination function (HCF) through DCF. The Clear-to-Send (CTS) and Contention-Free-End (CF-End) frames, introduced in earlier IEEE 802.11 amendments, are replaced with DMG CTS, DMG Denial-to-Send (DMG DTS), and DMG enhanced CF-End frames. Another large enhancement is the introduction of network allocation vector (NAV) timers. NAV timers indicate how long the channel is reserved for another STA and can be maintained for each pair of communicating STAs. When a STA receives a request-to-send (RTS) and a DMG CTS frames, it sets the NAV timer to the value provided in the duration field of the MAC header. STA may have one NAV timer per sector or it may utilize a single timer for all sectors. The medium is considered to be busy if at least one timer has a non-zero value. As an example, if a STA receives RTS frame addressed to itself while having a non-zero NAV timer(s) it may send a DMG DTS frame directly to the RTS frame originated STA. Note that this timer should not be mixed with the contention window timer which serves as the random access timer during CBAP. [4]. The length of the contention window depends on the category of the traffic. The IEEE 802.11 standard defines four different traffic/access categories. The further analysis of this medium access scheme is out of scope of this thesis.

The pseudo-static time division multiple access (TDMA) scheme allocates the available SPs, that occur every BI, to a specific STA pairs. Therefore, STAs need to request for channel time from the PCP, for example, during the CBAP. Not only has TDMA-based schemes proven to be highly robust and reliable in wireless communication systems but they also enable idle STAs to hibernate during access periods that are not assigned to them. This functionality is also implemented into the IEEE 802.11ad amendment under power save mode [4]. Especially with mobile devices with restricted power-supply this is very useful. According to the IEEE 802.11ad amendment, a STA requesting for a SP from the PCP must include the traffic type into the request. The requesting STA should define its traffic demand in terms of allocation duration, and isochronous or asynchronous traffic characteristics. To cal-

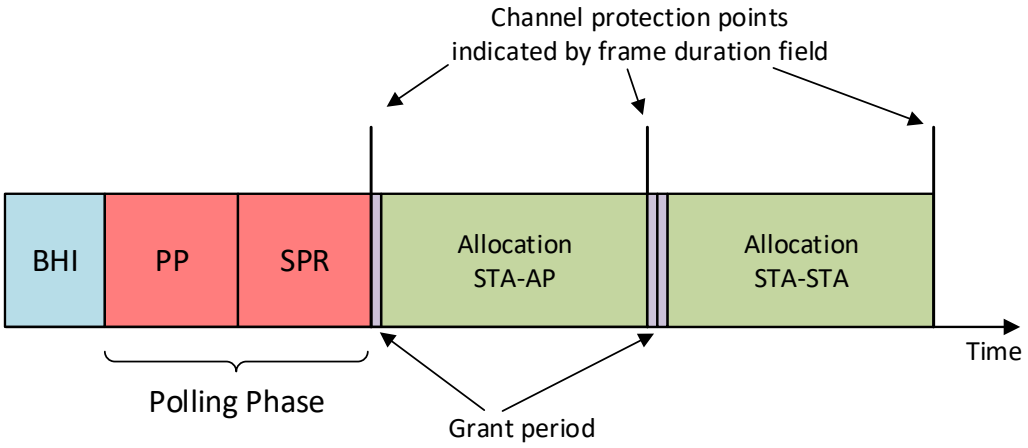

Figure 3.3 *Dynamic channel time allocation scheme. Adaptation of Fig. 4 in [34].*

culate the duration, the STA needs to have a trained link with known data rate. Traffic streams that are isochronous, such as wireless display streaming, may result in a pseudo-static SP allocation where the same pair of STAs receive SPs from every recurring BI. On the contrary, asynchronous streams do not require constant payload to be transferred. The actual SP allocations are broadcasted by the PCP in an extended schedule element in the BTI or ATI. [34].

The dynamic channel time allocation is a polling-based channel access scheme and is essentially an extension of the IEEE 802.11 point coordination function (PCF). Compared to the pseudo-static scheme, polling-based schemes are more flexible by nature. There are several advantages in polling-based schemes for millimeter wave communication. First, the deafness problem that is prominent in CBAP is prevented because the STAs are aware of the PCP direction due to centralized approach. Second, dynamic scheduling, compared to the pseudo-static scheduling, can adapt quicker to the alternating throughput demand as the channel time allocation can be altered in the course of the BI. [34].

The dynamic channel time allocation scheme is visualized in Figure 3.3. The procedure starts with a polling phase. First in the polling phase, the PCP sends polling frames to all STAs of the PBSS during a polling period (PP). Next, the polled STAs that want to request for channel access reply with service period requests (SPR). Consequently, the PCP then allocates the available SPs according to these requests

and sends grant frames to the associated STAs. Note that if the other participant of the SP is the PCP, only one grant frame is sent (to the non-PCP STA). To reduce implementation complexity and to simplify scheduling, dynamic allocations are scheduled in succession, in other words, each grant period is followed by its affiliated SP. If not all channel time is allocated during a single polling phase, the PCP can repeat the entire process. Otherwise, the remaining channel time can be used for CBAP.

Link adaptation is a dynamic mechanism for matching the modulation and coding scheme to the conditions of the radio link so that the data rate over the link will be maximized. Link adaptation through channel feedback was first introduced with the IEEE 802.11n amendment [39]. In IEEE 802.11ad, STAs can send link measurement requests to any STA it intends to communicate with [13]. In response, the feedback link measurement report contains the measured SNR in increments of 0.25 dB, recommended MCS, link margin, and an activity field. The activity field can be used to advise the requesting STA to: change MCS, decrease/increase transmit power, perform beamforming, and so on. The method by which the responding STA selects the recommended MCS is implementation specific. [4].

3.3 Directional Multi-Gigabit PHY Layer

The IEEE 802.11ad standard defines four different waveforms to be used in directional multi-gigabit (DMG) PHY [4]:

- *DMG control PHY* – Has to be implemented by the vendor as transmission and reception of control PHY PPDUs is mandatory.
- *DMG OFDM PHY* – Optional. Enables multiple carrier operation and increases spectral efficiency.
- *DMG SC PHY* – Mandatory. The transmission and reception of SC PHY PPDUs is mandatory for select MCSs. Provides relatively good spectral efficiency with low implementation complexity.
- *DMG low-power SC PHY* – Optional. For minimal power consumption and implementation complexity.

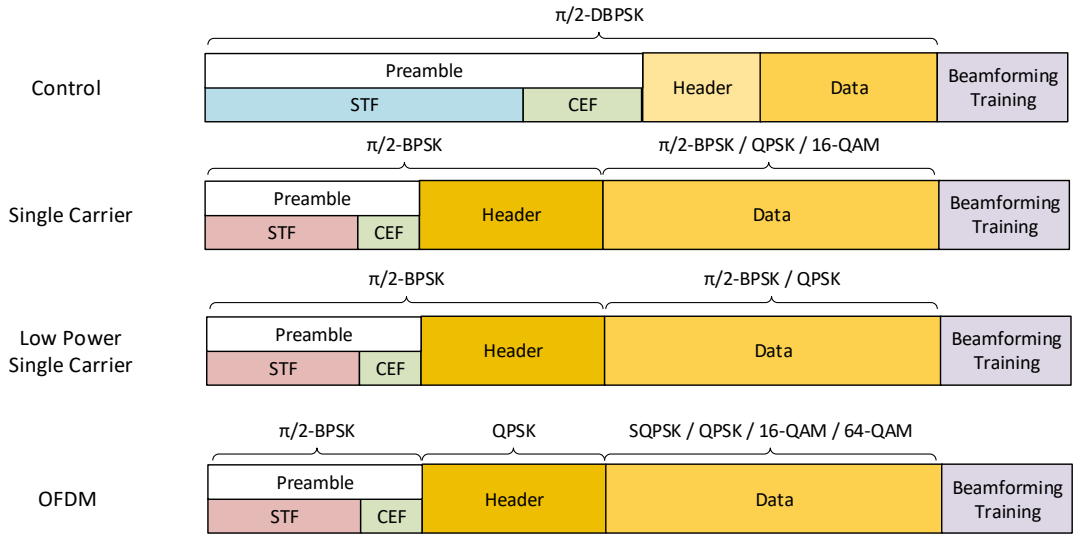

Figure 3.4 *IEEE 802.11ad frame structures.*

The fact that control PHY and SC PHY have to be implemented offers better co-existence between different vendor implementations and PHY mode configurations. Furthermore, the ability to choose between OFDM PHY and low-power SC PHY further broadens the variety of device configurations and use cases.

Figure 3.4 illustrates the frame structures for all previously mentioned PHY types. It can be seen that the different frame structures, excluding control PHY, are carefully aligned to simplify acquisition and processing in the receiver. The figure also shows the available modulation schemes. The more complex OFDM offers higher constellation modulation schemes which in return result in increased spectral efficiency. In contrast, robustness is much more important for the control PHY. Thus, differential binary phase shift keying (DBPSK) is used.

The preamble consists of a short training field (STF) and channel estimation field (CEF). The STF is used for automatic gain control (AGC), time synchronization, and frequency synchronization, whereas, the CEF is used for channel estimation. The preamble is constructed from repeating Golay sequences which are $\pi/2$-BPSK (binary phase shift keying) modulated. The $\pi/2$ appendix here means that the constellation is rotated by 90 degrees.

Following is the header field which defines the content of the rest of the packet. Simi-

larly as in the preamble, the control packet differs significantly from the single carrier and OFDM packets which resemble more one another. For normal data packets, the header is either $\pi/2$-BPSK or quadrature phase shift keying (QPSK) modulated, whereas, for the control packet is it $\pi/2$-DBPSK modulated due to robustness.

The packet payload, or data, contains the actual transferred information. To make sure that the encoding process produces integer number of modulation symbols, so called padding bits can be inserted to extend the payload data. The receiver can determine the number of dummy bits since the header describes the useful number of bytes in the payload. The specification includes 32 possible modulation and coding schemes (MCS). While this might seem like an excessive amount, the actual number of different modulation schemes and coding rates is much smaller.

Lastly, the antenna beamforming training field, consisting of antenna training fields (ANT), automatic gain control fields (AGC), and channel estimation fields, allows beamforming training for both participating STAs through beam refinement protocol (BRP) and beam tracking.

3.3.1 Preamble

Golay sequences are bipolar (± 1) sequences that have been mathematically constructed so that they have very specific cyclic autocorrelation characteristics. The characteristic dictates that for a complementary sequence pair of Ga_N and Gb_N, where N is the length of the bipolar sequence, the sum of their separate autocorrelation functions is zero, unless they are perfectly aligned. As an example, if $a = \{a_n\}_{n=0}^{N-1}$ for $a_n \in \{-1, 1\}\ \forall n$, then the corresponding autocorrelation function is:

$$R_a(k) = \sum_{n=0}^{N-k-1} a_n a_{n+k}, \qquad 0 \leq k \leq N-1 \tag{3.1}$$

The sequence pair is a Golay sequence pair if and only if:

$$R_a(k) + R_b(k) = \delta(k) \tag{3.2}$$

where $\delta(k)$ is the Kronecker delta function, which equals 1 at input 0 and is 0 with all other inputs [40]. This zero sidelobe characteristic is highly desirable as it enables channel estimation and synchronization without degradation. The IEEE

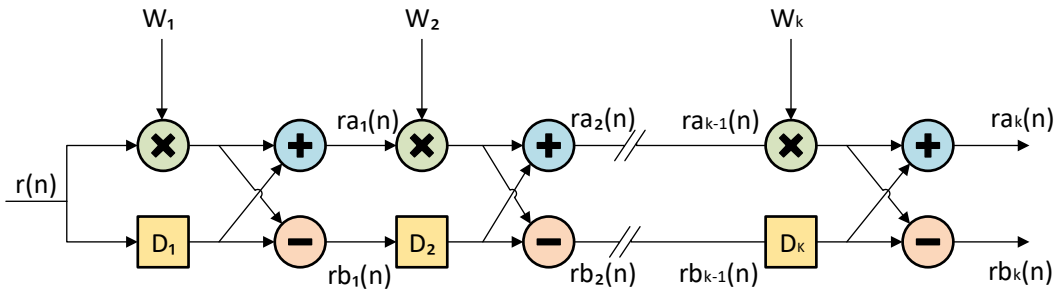

Figure 3.5 *Simple Golay correlator architecture.*

802.11ad specifies the following Golay sequences to be used: $\mathrm{Ga}_{128}(n)$, $\mathrm{Gb}_{128}(n)$, $\mathrm{Ga}_{64}(n)$, $\mathrm{Gb}_{64}(n)$, $\mathrm{Ga}_{32}(n)$, and $\mathrm{Gb}_{32}(n)$. These sequences are constructed using the following recursive algorithm:

$$
\begin{aligned}
A_0(n) &= \delta(n) \\
B_0(n) &= \delta(n) \\
A_k(n) &= W_k A_{k-1}(n) + B_{k-1}(n - D_k) \\
B_k(n) &= W_k A_{k-1}(n) - B_{k-1}(n - D_k)
\end{aligned}
$$

According to the standard, the previously mentioned Golay sequences are generated using this algorithm with these parametrizations [4]:

$$
\begin{aligned}
\mathrm{Ga}_{128}(n) &= \mathrm{A}_7(128 - n) & \mathrm{D}_k &= [1, 8, 2, 4, 16, 32, 64] \\
\mathrm{Gb}_{128}(n) &= \mathrm{B}_7(128 - n) & \mathrm{W}_k &= [-1, -1, -1, -1, +1, -1, -1]
\end{aligned}
$$

$$
\begin{aligned}
\mathrm{Ga}_{64}(n) &= \mathrm{A}_6(64 - n) & \mathrm{D}_k &= [2, 1, 4, 8, 16, 32] \\
\mathrm{Gb}_{64}(n) &= \mathrm{B}_6(64 - n) & \mathrm{W}_k &= [1, 1, -1, -1, 1, -1]
\end{aligned}
$$

$$
\begin{aligned}
\mathrm{Ga}_{32}(n) &= \mathrm{A}_5(32 - n) & \mathrm{D}_k &= [1, 4, 8, 2, 16] \\
\mathrm{Gb}_{32}(n) &= \mathrm{B}_5(32 - n) & \mathrm{W}_k &= [-1, 1, -1, 1, -1]
\end{aligned}
$$

It is important to notice that for both Ga and Gb the autocorrelations can be performed in parallel, using a relatively low complex correlator. Such a correlator is illustrated in Figure 3.5.

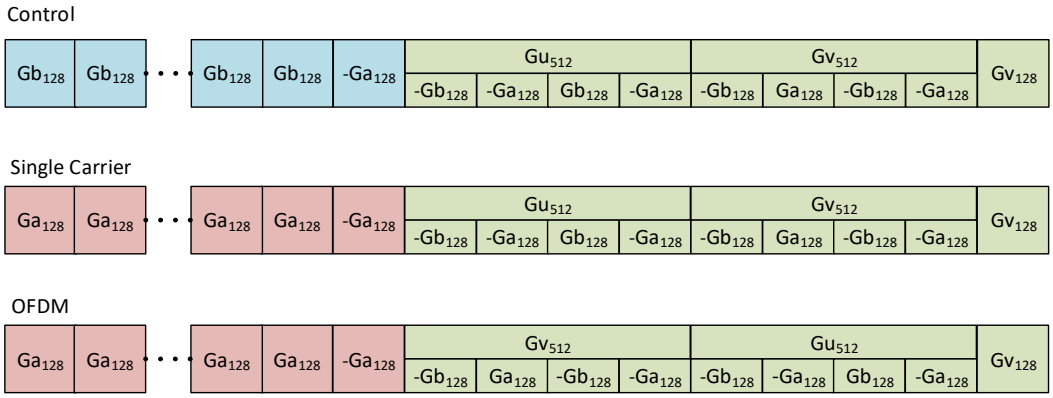

Figure 3.6 *STF and CEF of the available preambles.*

The correlator has a single input and two outputs, one for Ga sequence and the other for Gb sequence. For example, if a $\mathrm{Ga}_{128}/\mathrm{Gb}_{128}$ version of the correlator receives the preamble of a Control PHY, the output $\mathrm{rb}_7(n)$ would produce a positive correlation spikes, whereas, for SC PHY or OFDM PHY the output $\mathrm{ra}_7(n)$ would produce a positive correlation spikes. Therefore, due to the different STF sequences the receiver will know what frame structure to expect. Additionally, the frequency of the spikes gives a direct reference sample rate, the spikes amplitude can be used for AGC, and a negative correlation spike on the correlator output is used to signal the end of the STF.

Like mentioned earlier, the CEF is used for channel estimation but also for determining which modulation is used for the packet. Compared to STF, CEF is mathematically more sophisticated as it is made of a concatenation of two sequences $\mathrm{Gu}_{512}(n)$ and $\mathrm{Gv}_{512}(n)$. These sequences are defined as [4]:

$$\mathrm{Gu}_{512}(n) = [-\mathrm{Gb}_{128}, -\mathrm{Ga}_{128}, \mathrm{Gb}_{128}, -\mathrm{Ga}_{128}]$$
$$\mathrm{Gv}_{512}(n) = [-\mathrm{Gb}_{128}, \mathrm{Ga}_{128}, -\mathrm{Gb}_{128}, -\mathrm{Ga}_{128}]$$

The last 128 samples of these two sequences are equal to the last 128 samples used in the STF. The CEF ends with a $\mathrm{Gv}_{128}(n)$ which is equal to the first 128 samples of both $\mathrm{Gu}_{512}(n)$ and $\mathrm{Gv}_{512}(n)$, in other words, it is equal to $-\mathrm{Gb}_{128}(n)$. The modulation of the data field is determined by the order of the sequences Gu and Gv, as illustrated in Figure 3.6.

From the Figure it can be seen that when the data is OFDM modulated, the frame

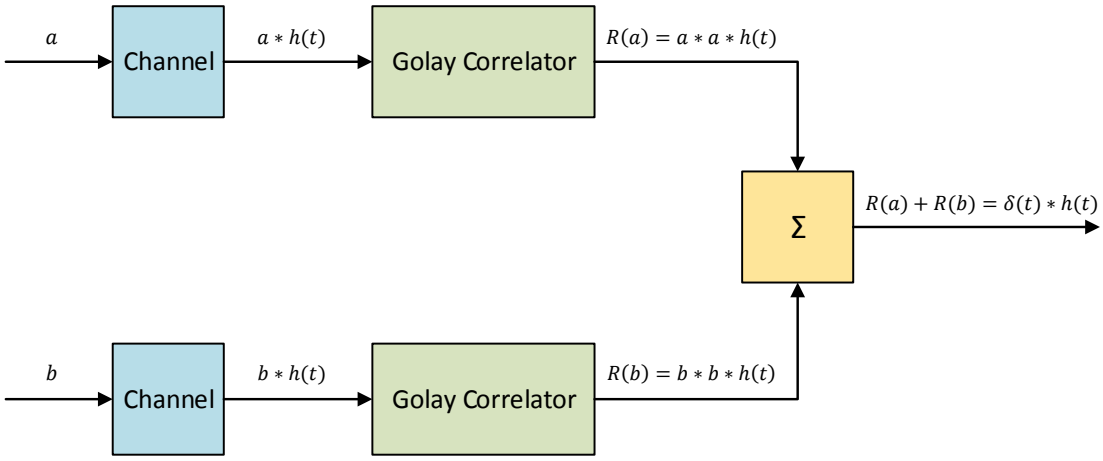

Figure 3.7 *Principle behind channel estimation using Golay sequences. Adaptation of a Figure in [35].*

structure is [Gv_{512}, Gu_{512}, Gv_{128}], whereas, for SC it is [Gu_{512}, Gv_{512}, Gv_{128}].

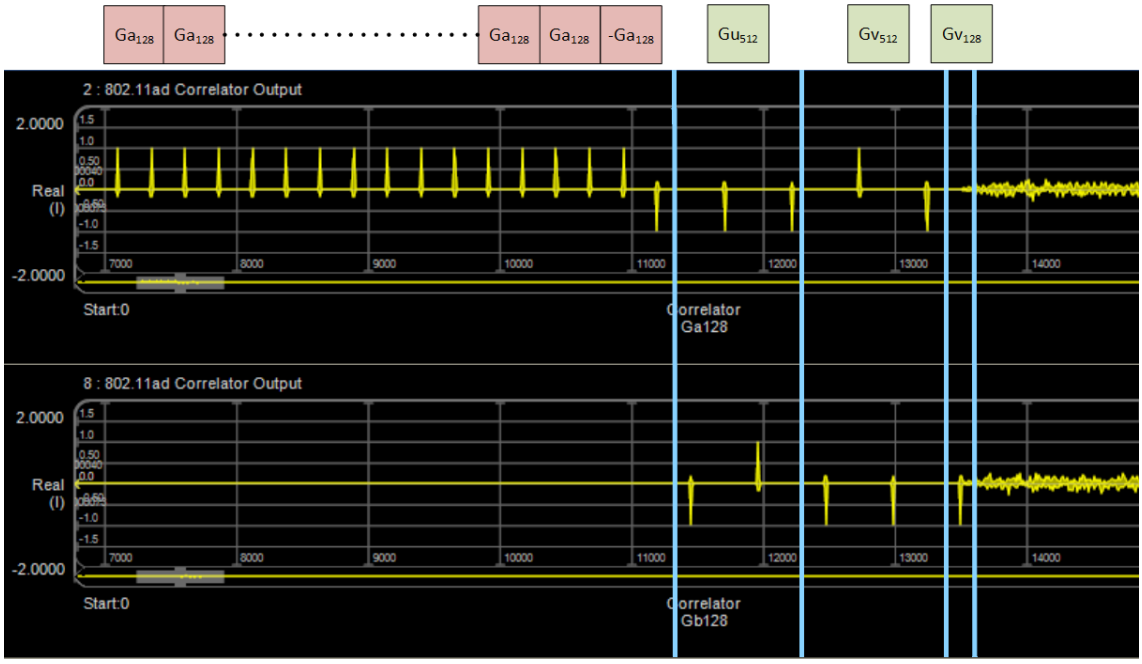

Figure 3.8 *Ga_{128} and Gb_{128} correlator outputs for Single Carrier PHY preamble. Adaptation of a Figure in [35].*

The basic principle of channel estimation is quite straightforward and takes advantage of the complementary nature of these sequences. This principle is presented in Figure 3.7. Let us assume two pre-known Golay sequences a and b. Feeding these through a channel corresponds to a convolution between the sequences and the channel's impulse response h(t). Now, as the sequences were known in the receiver, a Golay correlator will output an autocorrelation for both of these sequences convolved with the channel's impulse response. As was shown above, summing two autocorrelated Golay sequences together will result in a Kronecker delta function, and if the sequences are perfectly aligned, this will be equal to one. Subsequently, the receiver will end up with the channel response.

Figure 3.8 shows the Ga_{128} and Gb_{128} Golay correlator outputs for a SC PHY preamble. The repeating correlation spikes for the STF can be seen in Ga_{128} correlator output followed by a negative spike signaling the end of the field. This is then followed by the CEF.

3.3.2 Header

The preamble is followed by the header field which defines the details of the rest of the packet. Similarly as in the preamble, the control packet differs significantly from the single carrier and OFDM packets which resemble more one another. The PHY header contains the following [4]:

- *Scramble initialization*: seeding the scrambler which is used for whitening the rest of the packet.
- *Modulation and Coding Scheme (MCS)*: indicates the MCS used in the payload. Not used in the control PHY.
- *Length*: number of bytes in the payload.
- *Additional PPDU*: indicates whether or not an additional packet will be delivered next without standard frame spacing. Not used in the control PHY.
- *Packet type*: specifies if the packet contains beamforming training fields and of what type.
- *Training length*: length of the beamforming training field.

- *Aggregation*: indicates aggregation of multiple MAC layer frames into one PHY layer packet. Not used in the control PHY.
- *Beam tracking request*: indicates the need for beam tracking. Not used in the control PHY.
- *Tone pairing type*: indicates whether static or dynamic tone pairing is utilized. Only for OFDM PHY.
- *DTP indicator*: indicates if the dynamic tone pairing should be updated. Only for OFDM PHY.
- *Last RSSI*: indicates the last received signal strength indicator (RSSI). The used unsigned integer value does not directly specify the RSSI value in dBm, rather, a simple formula is used. Not used in the control PHY.
- *Header check sequence (HCS)*: checksum for validating the integrity of the header. This is based on a cyclic redundancy check (CRC 16-CCITT) error-detecting code.

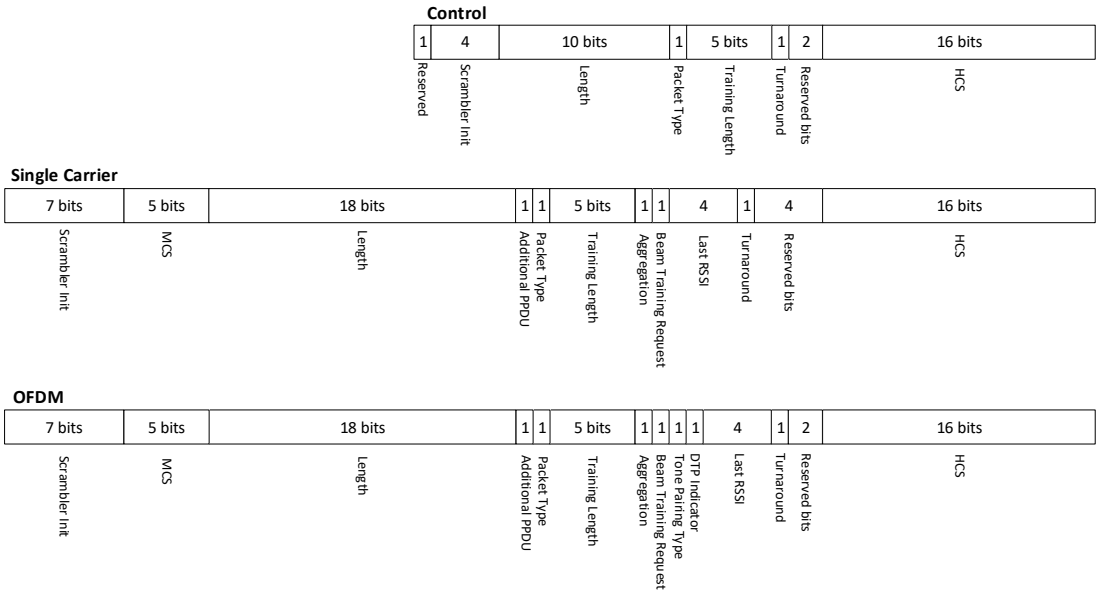

Figure 3.9 *IEEE 802.11ad header fields.*

All the available header field formats are shown in Figure 3.9.

3.3.3 Payload

The packet payload contains the actual transferred information. To make sure that the encoding process produces integer number of modulation symbols, so called padding bits can be inserted to extend the payload data. These dummy bits can be discarded at the receiver while decoding. The receiver can determine the number of dummy bits since the length field in the header describes the useful number of bytes in the payload.

The specification includes 32 possible modulation and coding schemes [4]. While this might seem like an excessive amount, the actual number of different modulation schemes and coding rates is much smaller. Therefore, representing the MCSs this way and dividing them into four PHY groups compresses the list significantly, as can be seen from Table 3.2.

Table 3.2 *Modulation and coding schemes in the IEEE 802.11ad. Reported bit rates are calculated only for the payload.*

	MCS	Channel Coding	Modulation	Bit Rate (Mbps)
Control PHY	0	Short $^{3}/_{4}$ LDPC, (32x spreading)	$^{\pi}/_{2}$ − DBPSK	27.5
Single Carrier PHY	1 to 12	$^{1}/_{2}$ LDPC (2x spreading), $^{1}/_{2}$ LDPC $^{5}/_{8}$ LDPC, $^{3}/_{4}$ LDPC, $^{13}/_{16}$ LDPC	$^{\pi}/_{2}$ − BPSK, $^{\pi}/_{2}$ − QPSK, $^{\pi}/_{2}$ − 16QAM	385 to 4620
OFDM PHY	13 to 24	$^{1}/_{2}$ LDPC $^{5}/_{8}$ LDPC, $^{3}/_{4}$ LDPC, $^{13}/_{16}$ LDPC	SQPSK, QPSK, 16-QAM, 64-QAM	693 to 6756.75
Low-Power Single Carrier PHY	25 to 31	*Outer code:* Reed-Solomon(224,208) *Inner code:* Block code(16/12/9/8,8)	$^{\pi}/_{2}$ − BPSK, $^{\pi}/_{2}$ − QPSK	626 to 2503

While it first might seem odd why so many different combinations of channel coding and modulation are used, but for the end user each incremental MCS step provides an increased throughput. This does not count the optional low-power SC PHY which can be seen as an alternative scheme for OFDM PHY, if low implementation complexity is preferred over high throughput.

3.4 Beamforming

Beamforming allows the communicating STA pair to train their receiver and transmitter antennas to achieve the required link budget for succeeding communication. While beam steering itself is not mandatory to be implemented, all devices should incorporate the associated MAC and beamforming protocols as they may communicate with other stations that do implement those features [13]. Consequently, the standard allows significant flexibility and has several optional features regarding beamforming [4]. Therefore, in this section the focus is on the mandatory parts of this procedure. The key steps of the procedure are: initial sector level sweep (SLS), beam refinement and beam tracking. This procedure, not including the tracking phase, is visualized in Figure 3.10. It is important to note that in the SLS phase, the responder sector sweep also contains feedback about the initiator sector sweep. Therefore, both participating STAs are able to determine both receiver and transmitter antenna system configurations.

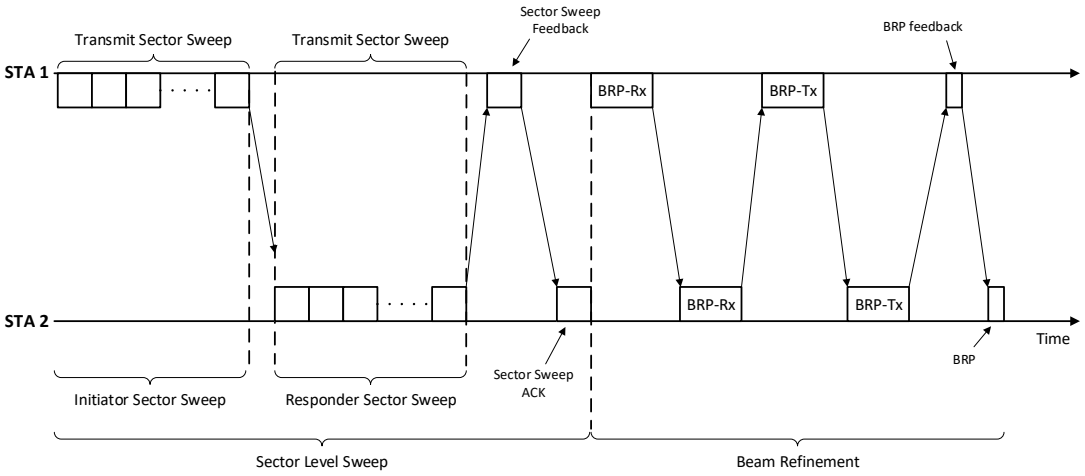

Figure 3.10 *Beamforming training procedure between two stations.*

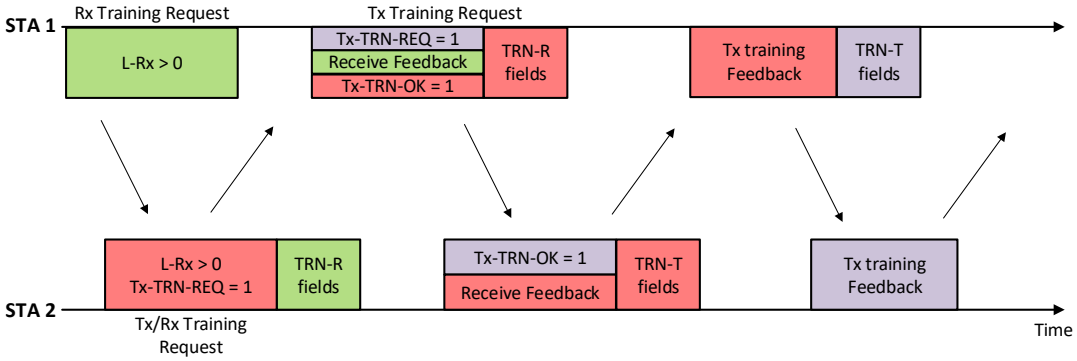

Figure 3.11 *Beam refinement mechanism (BRP). Adaptation of Fig. 7 in [34].*

First, initial sector level sweeps (SLS), which are bidirectional, allow both STAs to determine appropriate antenna system configuration for both transmission and reception. During a transmit sector sweep (TxSS), different beam sectors are used on each frame while the responding STA receives them with quasi-omnidirectional pattern. Each of these frames are marked with their corresponding antenna sector identifier so that the strongest sector can be identified. Feedback for the initiator is embedded to every responder TxSS frame to ensure the reception of this information under yet unknown antenna configuration. Finally, a sector sweep feedback is sent to the responder to confirm the optimum antenna configuration which is then accordingly acknowledged by the responder. The sector sweep acknowledge frame can include details about the following beam refinement. A receive sector sweep (RxSS) can be requested if the initiator knowns the capabilities of the responder. These capabilities can be obtained using information request and response procedure. During the RxSS, transmissions on the same sector allows to find the optimal receive sector similarly as described for the TxSS. [13].

Next, beam refinement using beam refinement protocol (BRP) may follow, if requested by either participating STAs. The purpose of this phase is to enable iterative refinement of the communication configurations found earlier in the SLS. In addition, BRP optimizes antenna weight vectors, which are independent of the predefined sectors, for phased antenna arrays. Although, these kind of antenna weight vectors may result in arbitrary antenna patterns, the directional nature with high throughput remains. Additionally, if RxSS was not performed in the SLS, the BRP can be used to find the optimum receive antenna configuration. BRP comprises two types of packets: BRP-Rx and BRP-Tx. These packets are PHY packets with

antenna training appended, like shown in the earlier section. BRP-Rx packets use TRN-R (receive training) sequences, whereas, BRP-Tx packets use TRN-T (transmit training) sequences. Total number of these sequences depends on the amount of different antenna settings desired to be explored. Figure 3.11 illustrates a BRP mechanism where first the receive configuration is refined, followed by a transmitter refinement. It is important to note how the STA 2 uses one packet for both Tx and Rx training, whereas, STA 1 uses two separate packets. Both of these methods are permitted by the specification. For the sake of understandability each request and the successive fields belonging to that request are marked with the same color. This phase is considered to be completed when the initiating STA determines that it does not need further training and that it has not received training requests from the responding STA. [34].

Finally, to keep the beams up to date as the propagation environment changes, beam tracking may be performed over a small set of antenna system configurations. Essentially beam refinement and beam tracking are the same procedure and both utilize the BRP. However, beam tracking refers to a smaller set of antenna configurations than the beam refinement. [13].

The association beamforming training (A-BFT) shown in Fig. 3.2 relies in the same procedure as was described above for the SLS. PCP uses the BTI during the beacon interval as the initiator sector sweep for all stations in the proximity. As unassociated stations cannot rely on coordinated communication, the following A-BFT interval implements a contention-based response period. The A-BFT interval is split into smaller slots for the participating stations, and the stations randomly select a slot. Collisions during the A-BFT interval are detected by missing feedback frames from the PCP. [34].

4. MEASUREMENTS

In this chapter we shall overview the measurement setup and the measurement scenario(s). The measurement results will be addressed in the following chapter. The purpose of these measurements is to evaluate and analyze the functionality and performance of an IEEE 802.11ad, also known as WiGig, system in a typical home environment. The analysis will mainly concentrate on the antenna array beam steering and beamforming side of things.

4.1 Measurement Setup

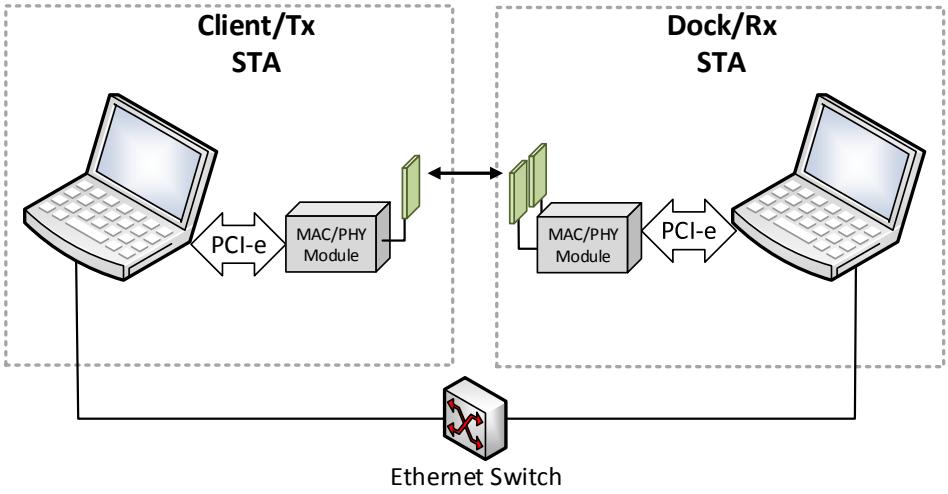

Figure 4.1 *Measurement setup.*

The measurement setup consists of two STAs, both having an external IEEE 802.11ad module, and an Ethernet switch. Purpose of this Ethernet link is to provide reliable connection for the performance testing software to exchange control information, in other words, number of packets sent/received, average error vector magnitude

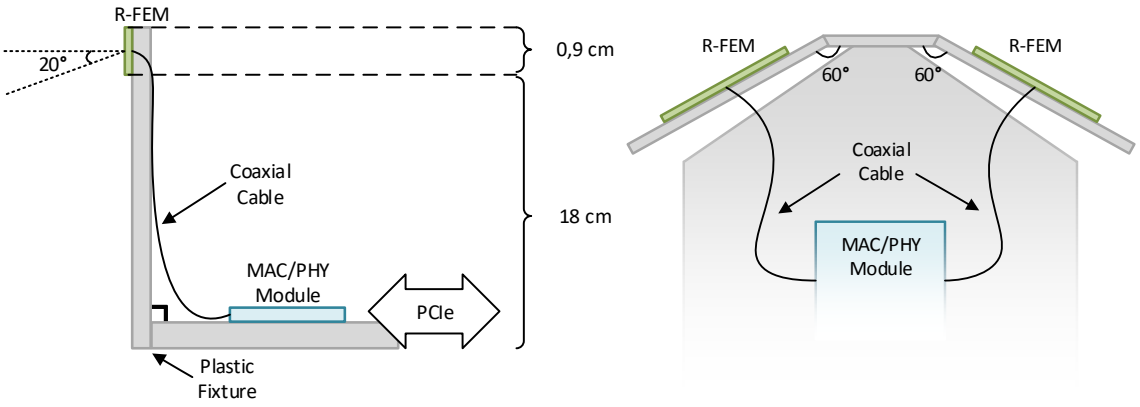

Figure 4.2 *(a) Side view of the client/Tx STA measurement fixture, and (b) top view of the dock/Rx STA measurement fixture.*

(EVM), average received signal strength indicator (RSSI) and so on. The external IEEE 802.11ad module is communicating with the laptop through Peripheral Component Interconnect Express (PCIe) bus. The measurement setup is visualized in Figure 4.1. As can be seen from the Figure, there are some small differences between the client STA and the dock STA. The noticeable difference being that the dock STA supports dual radio front-end modules (R-FEM) which extends the coverage.

The module itself comprises two distinct parts: an IEEE 802.11ad MAC/PHY module, and a R-FEM. The R-FEM contains a radio frequency integrated circuit (RFIC), which supports all IEEE 802.11ad channels except channel four, and a 16-element antenna array. The antenna configuration is a phased array, similar to the one presented in Fig 2.9, that coherently combines to form a single beam, thus focusing all transmitted radiation in a single direction towards the receiving STA to enable increased range, high throughput and low interference. Mounting of the client/Tx and dock/Rx STA R-FEMs is shown in Figure 4.2. The Tx STA fixture tries to mimic an actual end product, for example a laptop, where the R-FEM could be mounted to the edge of the screen panel. This is an optimal place for the antenna as it is elevated above the surface on which it is placed upon. Obviously, there are numerous benefits caused by this elevation. As was mentioned in the previous chapters, 60 GHz signal propagation can be described to be quasi-optical, where the LOS and first order reflection paths are the most dominant paths to the receiver. Now, as the antenna is elevated, the likelihood for the LOS path to obstructed decreases as less objects are between the Tx and the Rx antennas. In comparison, the dock/Rx

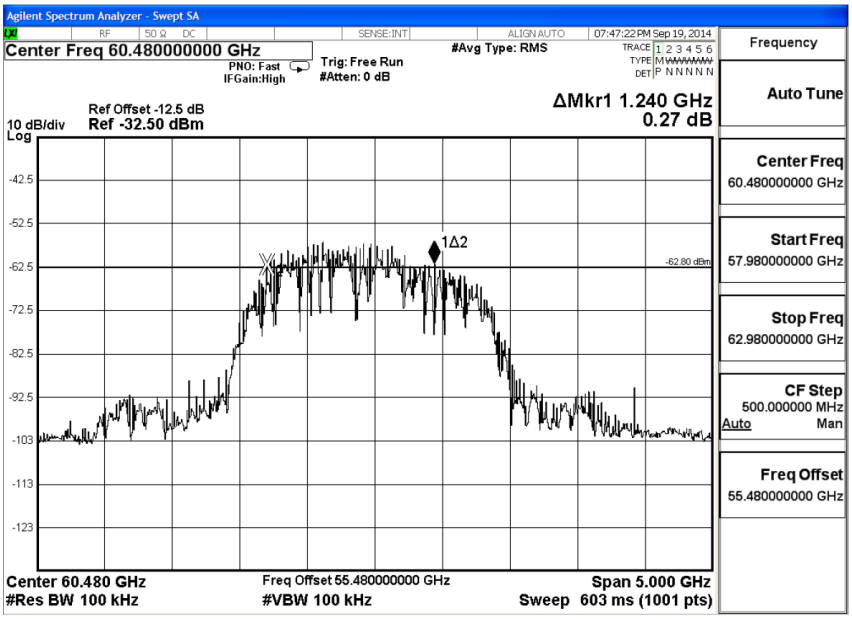

Figure 4.3 *Measured 6 dB bandwidth of the IEEE 802.11ad signal at channel 2 [41].*

STA R-FEMs have been mounted to a 60 degrees angle and they have been elevated only by 7 cm. Like illustrated in the Figure, the antenna array itself has a natural beam tilt of 20 degrees downwards to improve spatial coverage. It should be noted that in an actual implementation, the beamforming mechanisms of antenna arrays make the mechanical design of the device more difficult. Normally all antennas are embedded inside the mechanics so that they are not visible outside. The so called coverage loss may easily occur if the mechanics are blocking the antenna radiation in some directions. Nonetheless, in our implementation antennas are placed on top of the dummy mechanics to ensure non-obscured coverage.

Table 4.1 *General information and capabilities of the module.*

Supported MCS	Output Power	Antenna Gain	EIRP	f_{RF} [GHz]	f_{IF} [GHz]	f_{Clock} [GHz]
0–12	10.25 dBm	15.45 dBi	25.70 dBm	60.48±2.14	10.56	1.32

The MAC/PHY module implements the IEEE 802.11ad SC PHY with the mandatory Control PHY. Hence, like it was shown in the Table 3.2 of the previous chapter, the maximum MCS available will be MCS 12 which gives a theoretical max through-

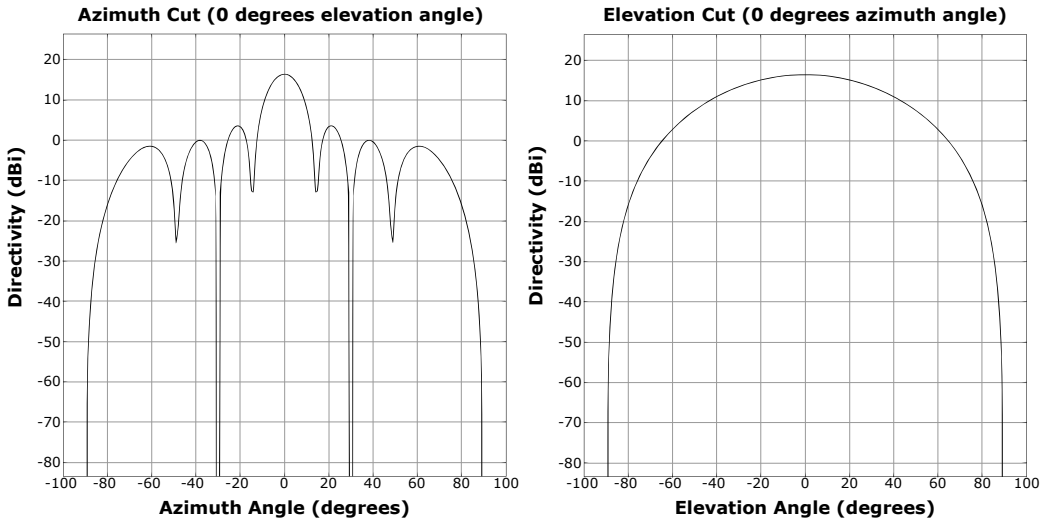

Figure 4.4 *Simulated antenna array directivity when the antenna array is not steered.*

put of 4.62 Gbps. Table 4.1 comprises the general information of the module. The given power and gain values are actual measured values.

Measured spectrum of the IEEE 802.11ad signal at channel 2 is shown in Figure 4.3. Channel 2 was particularly chosen as it is globally available, as was mentioned in Chapter 2. Consequently, all following measurements are conducted at this channel. The measured 6 dB bandwidth at this channel is 1.24 GHz. Comparing this Figure to the spectrum mask (Fig. 2.2) it can be seen that the module fulfils this spectral requirement placed by international regulatory bodies. Due to the fact that the IEEE 802.11ad module is intellectual property of Intel Corporation, further architectural decisions and implementation details cannot be presented here.

Simulated antenna array directivity is shown in Figure 4.4. The simulation assumes uniform rectangular array configuration, in other words 2 by 8 antenna array, which consists of isotropic antenna elements that are backbaffled. Backbaffling here means that the element does not radiate backwards. The elements are spaced 0.5 wavelengths apart in both directions. The main beam of the antenna array has roughly 16 dBi gain and a 3 dB beamwidth of 13 degrees in azimuth plane. The Equation (2.13) gives roughly the same beamwidth, and the Equation (2.12) gives an approximation of 15.7 dBi gain assuming array efficiency of 0.75 and an element length of 1.04 mm in azimuth plane. In the elevation plane the antenna array performs similarly to a backbaffled omnidirectional antenna. Although from the figure it can be seen

that the antenna array has a strong directivity, relatively strong sidelobes are still present. At this orientation, strongest sidelobes are located at ±21 degrees with −13 dBr power compared to the main beam. These sidelobes are further amplified in contrast to the main lobe when the antenna is steered. Additionally, as was discussed in the previous chapter, grating lobes will start to degrade the directivity of the antenna at large steering angles. In this prototype, the main beam can be steered ±60 degrees in both planes. As was described in the previous chapter, the relation between antenna element spacing and maximum steering angle is (Equation 2.11):

$$d \leq \frac{\lambda}{1 + \cos\theta_{max}} = \frac{\lambda}{1 + \cos(90° - 60°)} = 0.54\lambda$$

thus, the element spacing of 0.5λ will fulfil this requirement and no grating lobes should be introduced by this antenna array. But as we will see, this approximation is not valid for small antenna arrays, like the one that is used in this thesis. Of course these simulations do not perfectly model the actual antenna array but they will give us a reasonable estimate about the radiation pattern at various steering angles.

4.2 Measurement Scenario

Measurements at 60 GHz have been conducted earlier in laboratory and office/conference room environments. However, in these scenarios the environment has been made favorable for the measurements as very little obstacles have been present. Few examples of these measurements are provided in [7–12].

In contrast to these measurements, most end-user devices will be operated at environments that are much more cluttered than the environments used in the previously mentioned measurements. An average conference room typically only has a table and few chairs. All furniture are roughly on the same height and most walls are not covered by any paintings or cabinets. On the other hand, there is no standard for a living room. You may find various tables, sofas, chairs, cabinets, paintings, (floor) lamps, rugs et cetera. Thus, understanding 60 GHz communication in this environment becomes increasingly interesting. Therefore, measurements conducted for this thesis were done in a home environment.

Figure 4.5 shows a simple computer-aided design (CAD) of the main measurement

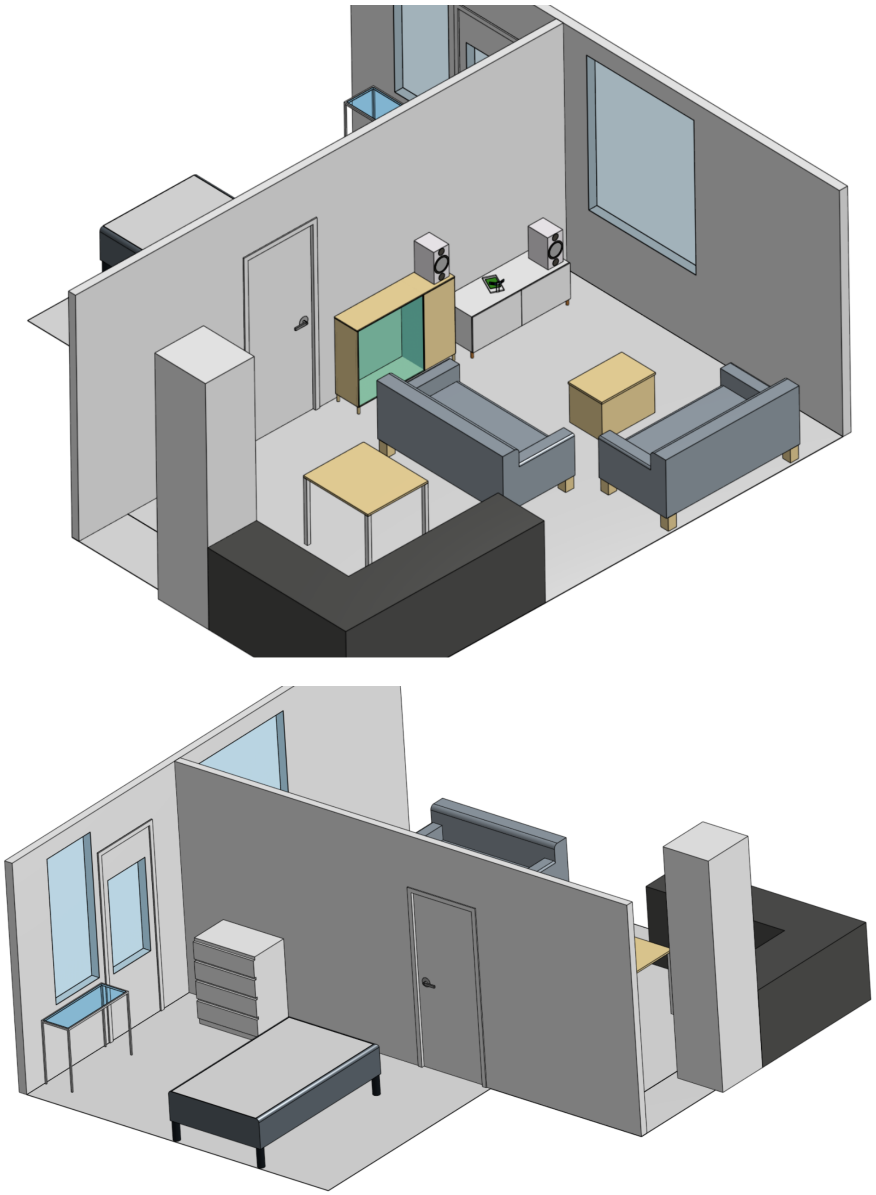

Figure 4.5 *Computer rendering of the measurement environment.*

scenario. As has been mentioned earlier, due to the quasi-optical nature of signal propagation at 60 GHz, the impact of reflecting surfaces is massive. Hence, a CAD rendering of the measurement environment helps us better understand the possible propagation paths. For analyzing the results, the rendering gives much more information of the measurement environment than photographs as it can be rotated and manipulated in ways that photographs cannot be. From the rendering one can see the large objects that potentially can block the LOS path and cause distortion to

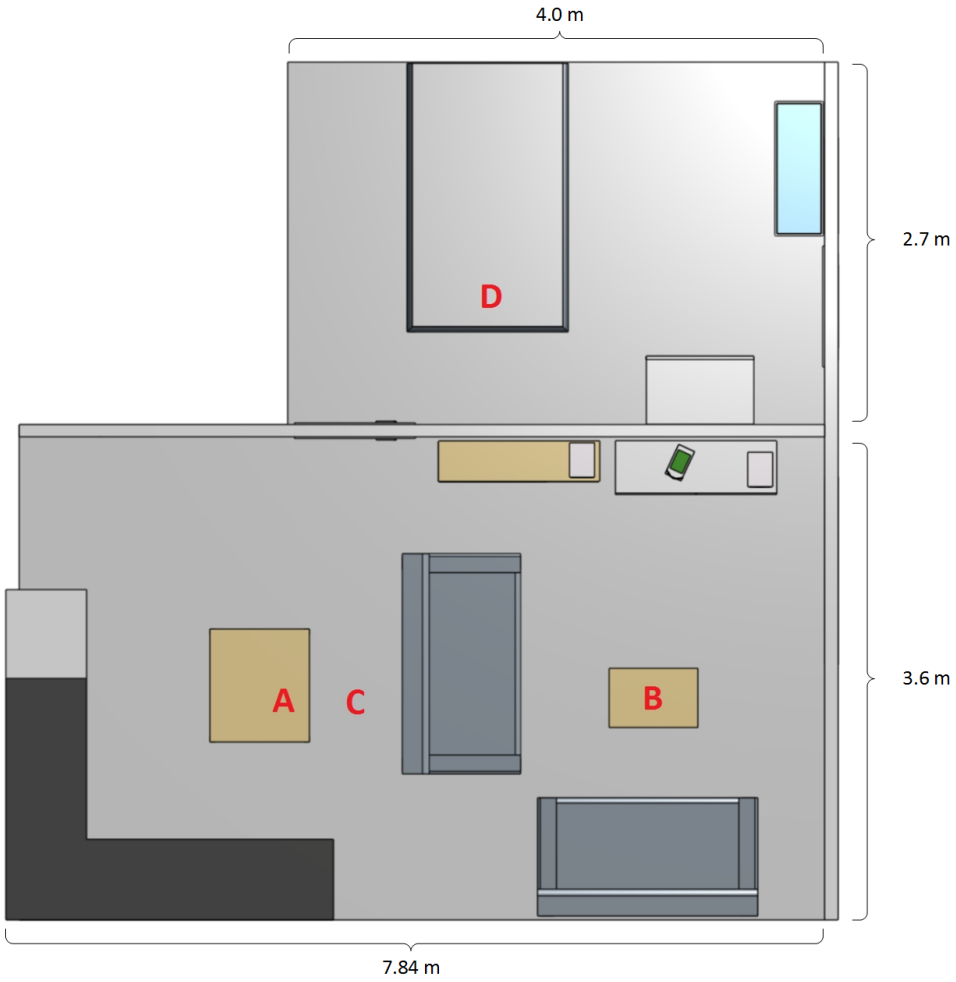

Figure 4.6 *Measurement locations.*

the signal. On the other hand, there are some nice reflecting surfaces, such as, the large window and the glass panel of the bookshelf. It could also be assumed that the smooth walls could work quite nicely as reflecting surfaces. The dock/Rx STA is located on top of the TV bench as is shown in the Figure.

The measurements were conducted in various places around the room. These measurement points are marked to the Figure 4.6 with alphabets. It should be emphasized that only the client/Tx STA is moved around the room, whereas, the dock/Rx STA stays stationary (excluding one measurement). This mimics the typical home use case where the dock device is (most of the time) stationary in one place and the terminal device is moving with the user. Like it was mentioned in the previous chapter, it has been predicted that one of the most typical use cases for IEEE

802.11ad will be lossless display streaming to a monitor or a TV. Thus, the dock-/Rx STA would be close (or build in) to the monitor/TV and the mobile streaming device (Tx/client STA) would move with the user. From these assumptions one can already argue that the dock/Rx STA will most likely be oriented and placed in a much better way compared to the mobile client/Tx STA. Hence, understanding how the beam steering and beamforming protocols perform in these not-so-optimal locations and device orientations becomes one of the key factors on maximizing the achievable throughput.

Table 4.2 *Spatial information about the measurement locations (see Fig. 4.6).*

Measurement point	Tx elevation [m]	Rx elevation [m]	Δh [m]	Distance [m]	LOS
A	0.73	0.56	0.17	3.44	Yes
B	0.44	0.56	0.12	1.67	Yes
C	0.00	0.56	0.56	2.70	No
D	0.55	0.56	0.01	~2.00	No
A	0.73	**1.79**	1.06	3.44	Yes

Table 4.2 shows the spatial information related to each measurement point which were shown in the earlier Figure. Δh denotes the absolute elevation difference between the Tx and Rx STAs, and the LOS parameter indicates whether or not a LOS path is available. In the measurement point "D", the given distance is an estimate due to the wall between the STAs. In the last line of the Table is a measurement case where the Rx STA is elevated closer to the ceiling to emulate a device which are typically installed directly to the ceiling or a wall close to it, for example, a projector or a loudspeaker.

5. RESULTS AND ANALYSIS

In this chapter, the measurement results are presented and further analyzed. As previous practical academic work in millimeter waves has focused on measurements in laboratory or office environments, these measurements were conducted in a home environment as was described in Chapter 4 which also described the measurement setup.

These measurements can be divided into two categories: (manual) beam steering measurements and beamforming measurements. The beam steering measurements focus more on the capabilities and characteristics of the antenna array itself, whereas, the beamforming measurements focus on the performance of the implemented beamforming algorithm and, thus, the modem. The theory of antenna array beam steering was discussed in detail in the Section 2.3.3 and the IEEE 802.11ad beamforming protocol was addressed in Section 3.4.

5.1 Manual Beam Steering Measurements

To better understand highly directional communication at millimeter waves, sweep measurements were conducted in various locations. In these measurements, both STAs are aligned towards each other and stay stationary during the measurement. Then, the main beam is steered in azimuth plane for both STAs.

RSSI distribution from measurement point "A" (the kitchen table) is shown in Figure 5.1. As the two STAs are aligned, it is obvious that the most illuminated area is found when both beams are not steered. However, it can be seen that there is a slight off-set in Rx azimuth which is most likely due to the fact that the Rx antenna array is not ideally aligned. Yet, this is a relatively small off-set. There are three other illuminated areas in the figure when the Tx azimuth is set to zero. These are caused by the Rx sidelobes at 0 degrees azimuth when the Rx beam is steered. Consequently, notches are seen when a sidelobe is not located at the 0 degrees azimuth,

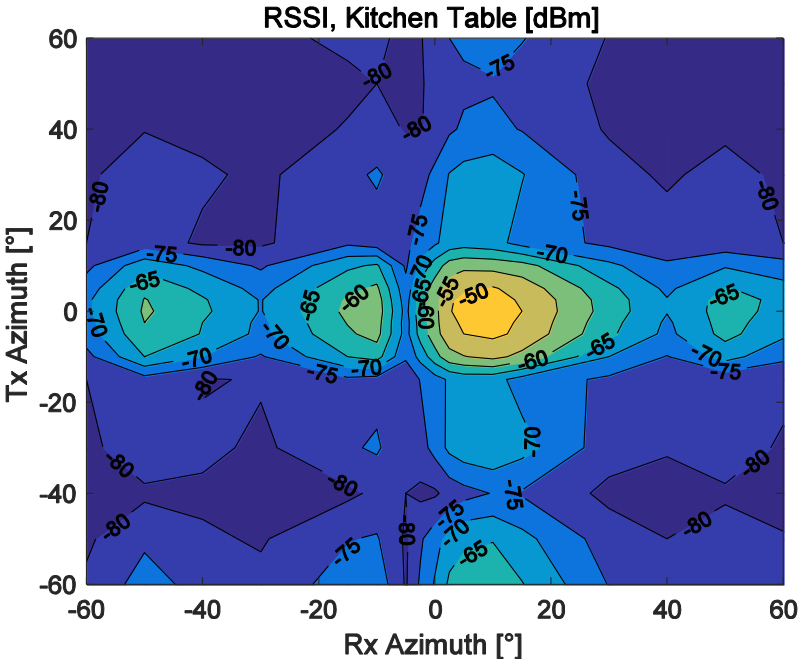

Figure 5.1 *Distribution of RSSI as a function of transmit and receive antenna azimuth for the measurement conducted at measurement point "A" (see Fig. 4.6). Elevation is set to 0° for both Tx and Rx.*

for example, when the beam is steered by ±30 degrees azimuth. According to the antenna array simulations, these Rx sidelobes have roughly $13 - 15$ dB less power than the non-steered beam, which is also what the results suggest if compared to the LOS case with -50 dBm RSSI.

The last illuminated area can be seen in the bottom part of the figure, that is, when the Tx azimuth is roughly -60 degrees and Rx azimuth is roughly 10 degrees. Now, it is important to remember that as the antenna array beam is steered, the radiation pattern changes quite drastically. This can be seen from Figure 5.2 in which the same antenna array is steered -60 degrees in azimuth plane. Especially at 90 degrees azimuth there is a strong sidelobe that has -9 dBr power compared to the non-steered main bream (Fig. 4.4). This sidelobe is reflected from the concrete wall that is opposite of the receiver (Fig. 4.5). According to the Table 2.1, concrete with small angles of incidence (angle between the incident wave and the normal of the surface) has a reflection loss between 6 and 7 dB. This analysis is supported by our experimental measurements as it can see that the RSSI from this reflected sidelobe is roughly 15 dB lower than on the non-steered LOS case.

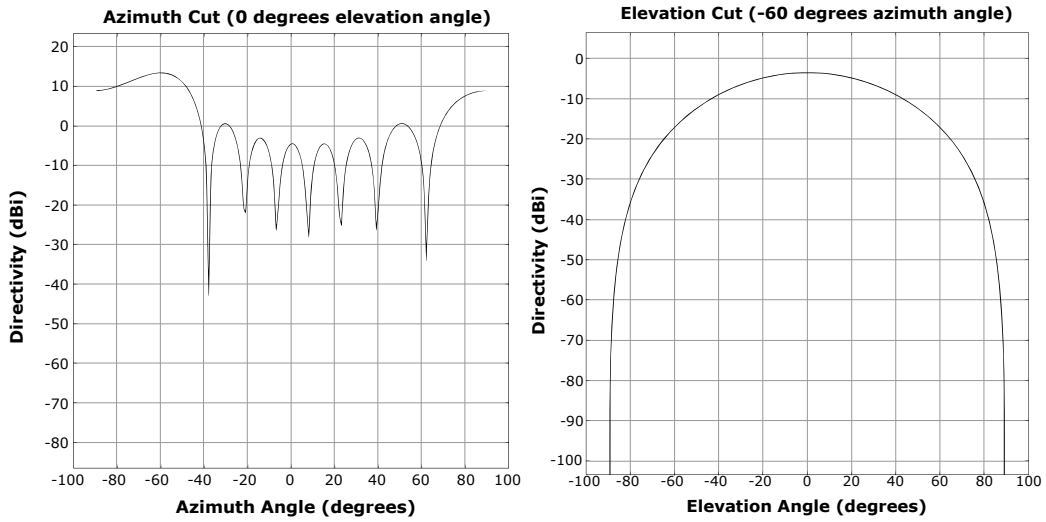

Figure 5.2 *Simulated antenna array directivity when the antenna array is steered in azimuth plane by* -60 *degrees.*

Similar results can be seen from the sofa table case (Fig. 5.3). In this case the distance between the STAs is smaller and therefore the RSSI values are higher across the board. Similarly as in the previous case, the Rx sidelobes are visible at ± 20 degrees and ± 60 degrees Rx azimuth when the Tx azimuth is set to 0 degrees. Likewise, the illuminated area at the bottom part of the figure (Tx is steered -60 degrees azimuth) is caused by a sidelobe. However, this time the sidelobe in question is located at 0 degrees azimuth with roughly -20 dBr power compared to the non-steered main bream (Fig. 4.4). As it can be seen from the results, in reality the value is actually -15 dBr. Most interestingly, the illuminated area in the top part of the Figure (when Tx is steered by 60 and Rx by -60 degrees) is most likely caused by a main beam partially reflecting from the window. Smooth glass surfaces typically have high reflection losses with small angles of incidence (Table 2.1) as the signal easily penetrates this type of a material. From the Table we can estimate that a 10 dB reflection loss is to be expected. Additionally, the steered main beam is roughly 3 dB weaker than its non-steered counterpart. The measurement result concludes that the actual losses are in the proximity of 15 dB which is reasonably close to what the simple analysis suggested. The same reflection path can be seen in the bottom part of the Figure, when both the Tx and the Rx are steered -60 degrees azimuth. Again, according to Figure 5.2, a sidelobe is located at 50 degrees azimuth with roughly -11 dBr less power than the main beam. Another possibility is the strongest sidelobe at 90 degrees as it has quite a large beamwidth. All the same,

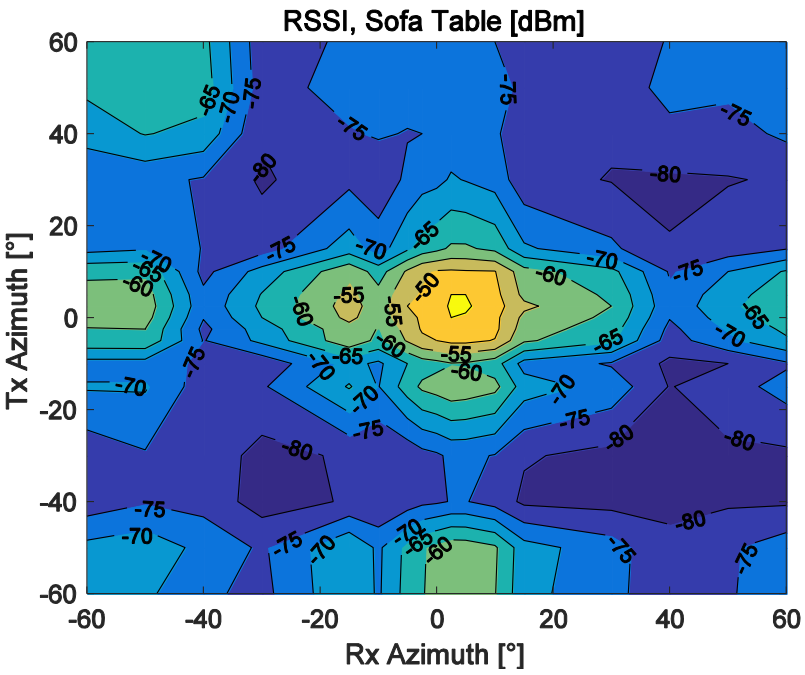

Figure 5.3 *Distribution of RSSI as a function of transmit and receive antenna azimuth for the measurement conducted at measurement point "B" (see Fig. 4.6). Elevation is set to* 0° *for both Tx and Rx.*

the measurement result suggests that this sidelobe would only be −5 dBr weaker than the main beam in the previously mentioned steering configuration. However, it should be kept in mind that the incident angle towards the glass might not be the same, and therefore the reflection loss could be completely different.

As some devices, such as projectors and loudspeakers, are installed much higher and closer to the ceiling, measurements were also conducted so that the Rx STA was elevated closer to the ceiling (see Table 4.2). Mainly the motivation was to study what kind of effect the ceiling has and also what happens if the STAs are not in the same horizontal plane. The measurement results are presented in Figure 5.4. To better understand the antenna steering in elevation plane, the Rx STA was steered by −30° in elevation plane. This should also increase the peak RSSI value in the measurements. Straight away it is obvious that the results resemble the earlier results when the Rx STA was not elevated (Fig. 5.1), as the measurement setup and location are almost identical. However, because the Rx STA was steered in elevation plane, the RSSI pattern is somewhat different. It almost looks like the results are mirrored along the 0 degree line at Tx azimuth.

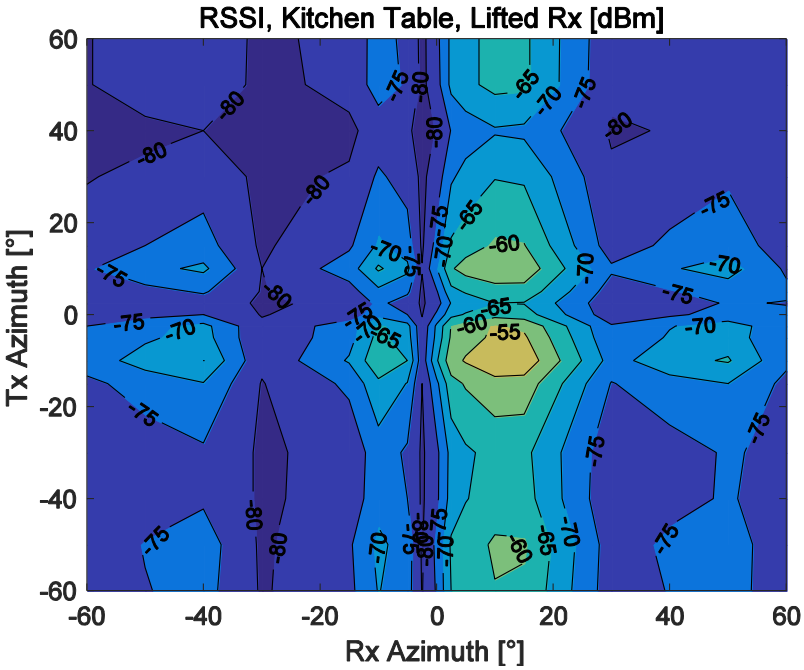

Figure 5.4 *Distribution of RSSI as a function of transmit and receive antenna azimuth for the measurement conducted at measurement point "A" (see Fig. 4.6). Elevation is set to* $0°$ *for Tx and and* $-30°$ *for Rx.*

The explanation for this lies in the steered Rx antenna pattern which is shown in Fig. 5.5. As it was shown in the earlier chapters, the performance of a beam steerable antenna array increases as more elements are introduced. For example, with two elements it is intuitive that there are two phase fronts which sum up constructively at the steering angle, destructively in the "middle", and then there is a sidelobe. Now, if the number of elements is increased the destructive interference reduces the beamwidth of the main beam, and reduces the sidelobe, but also introduces more sidelobes. In other words, higher complexity equals tighter main beam and weaker sidelobes. Consequently, as our antenna array is two rows of eight elements the performance of beam steering in elevation plane is limited, as can be seen. There are few things that need to be highlighted from these results. First, even though the peak RSSI value is few dBs lower than in the non-elevated scenario, the average RSSI levels are higher when the Rx azimuth is between 0 and 20 degrees. Second, these illuminated areas are larger than in the non-elevated scenario. It is hard to find an explicit reason for these two things but it is safe to say that, as the Rx STA is elevated, less objects are blocking the Fresnel zones between the STAs. Hence, the potential destructive interference caused by these objects in the Fresnel zones is

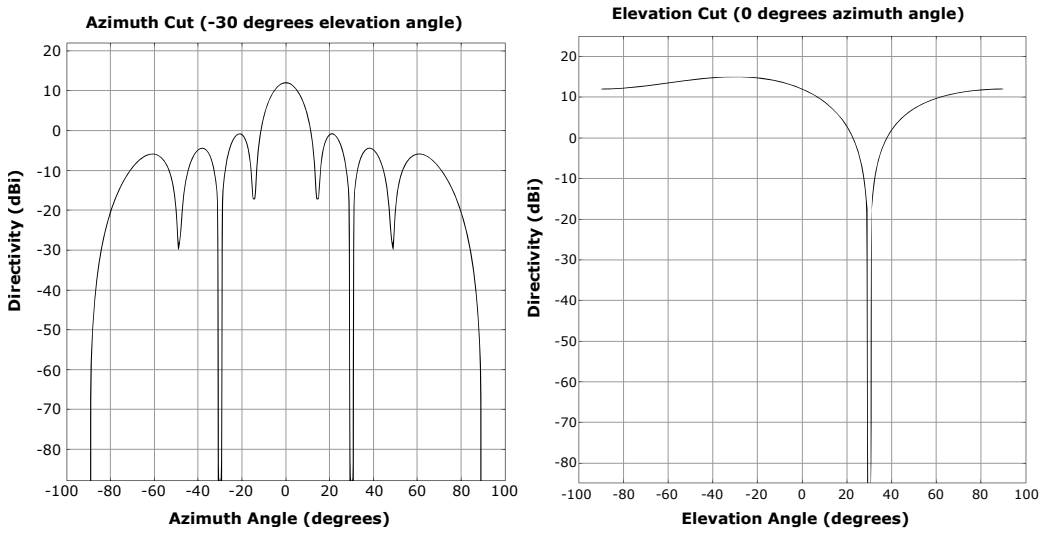

Figure 5.5 *Simulated antenna array directivity when the antenna array is steered in elevation plane by* -30 *degrees.*

neglected and the RSSI results are overall improved.

While RSSI values give some idea about the system performance, MCSs explicitly define the system throughput and thus the end-user performance. Hence, measurements were carried out in similar fashion as in Fig. 5.1 but now focusing on the maximum achievable MCS. As it is to be expected, these results (Fig. 5.6) are in line with the previous RSSI results. High RSSI values indicate good channel conditions and thus high throughput. It can also be seen that, even though the illuminated areas in the RSSI measurements were relatively small, decent throughputs can be achieved from a wider area of angles. For example, if the Tx STA is steered towards the Rx STA, the minimum expected MCS is more or less around 8, equaling 2.3 Gbps throughput. In comparison, the maximum theoretical throughput of the IEEE 802.11n standard is 600 Mbps. Furthermore, even higher throughputs could be achievable in this measurement scenario because, like was mentioned earlier, the prototype only implemented MCSs up to 12.

Finally, measurements were conducted from one room to another to better understand the performance through a wall and also to see if an open door serves as a better propagation path. The wall in question is a non-load bearing wall made out of plasterboard. It should be noted that in these measurements the Rx STA was relocated on top of the sofa table (measurement point “B”) so that the reflecting

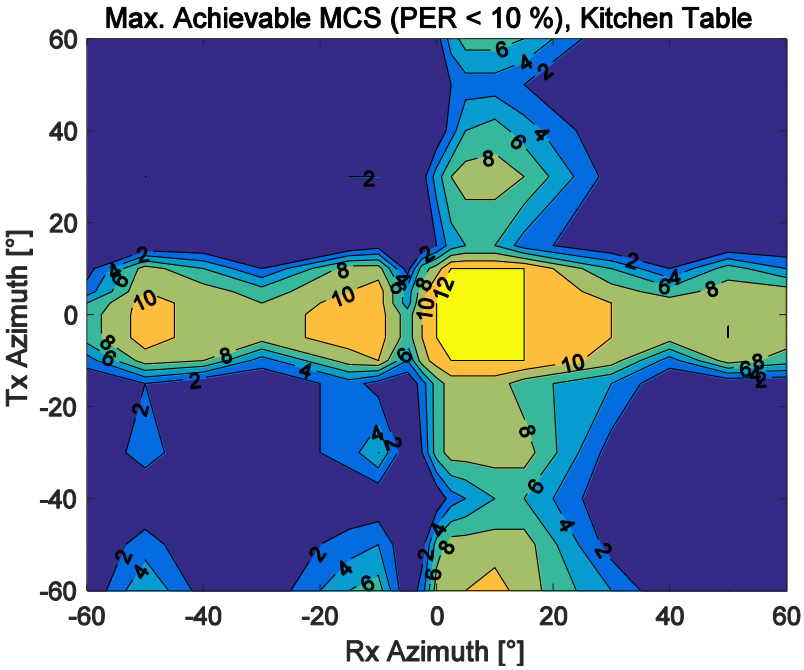

Figure 5.6 *Maximum achievable MCS as a function of transmit and receive antenna azimuth for the measurement conducted at measurement point "A" (see Fig. 4.6). Elevation is set to* 0° *for both Tx and Rx.*

path from the open door would be more feasible. The Tx STA location in this measurement is marked with "D" (see Fig. 4.6). The measurement results are presented in Figure 5.7.

From the results, it is obvious that the performance in these types of scenarios would be greatly impaired. Assuming similar smooth plasterboard as in Table 2.1, we already get roughly 6 dB attenuation from the wall itself (assuming angle of incidence of 0 degrees). However, the angle of incidence in this case is much larger than 0°, the plasterboard used might be thicker, and the insides of the wall are not known. Pipes and cables inside the wall can easily introduce additional losses. Additionally, the bookshelf and the two cabinets are partly obstructing the propagation path through the wall. Comparing the illuminated area to the CAD model, it can be seen that the strongest propagation path goes near the edge of the cabinet. This suggests that the glass front of the bookshelf is strongly trapping and reflecting the wall penetrated signal, whereas, the wooden side compartment introduces much less losses. It could also be argued that the small cap between the bookshelf and the cabinets is the path offering least losses. One key finding from these results is that the open door

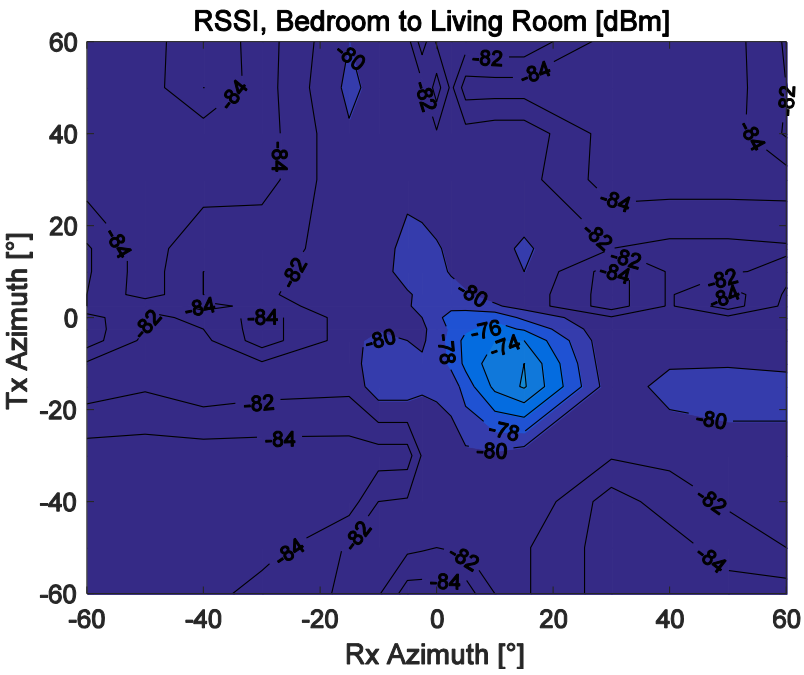

Figure 5.7 *Distribution of RSSI as a function of transmit and receive antenna azimuth for the measurement conducted at measurement point "D" (see Fig. 4.6). Elevation is set to* 0° *for both Tx and Rx.*

path does not show up at all in the results. Few things could be said about this. First of all, the door is hollow and made of thin fiberboard. Now, as we know from plasterboard, these types of materials have really high reflection losses with steep angles. In our case the angle is somewhere around 20 to 30 degrees, which on smooth plasterboard equals roughly 10 dB reflection losses. Most of the signal is probably penetrating the door entirely. Second, the sofa is partly obstructing the reflection path from the door to the Rx STA. Therefore, the results make sense.

5.2 Beamforming Measurements

Next, measurements were performed to analyze the beamforming performance of the module. The measurements were conducted so that the Rx STA stays stationary, similarly as earlier, but now the Tx STA is rotated along its yaw axis. Yaw axis is essentially the vertical axis that is perpendicular to the object and goes through the center point of the object. 0 degrees angle means that the Tx STA is pointed toward the Rx STA. Positive angles rotate the antenna array clockwise and negative angles counterclockwise. It needs to be highlighted that in these measurements, the

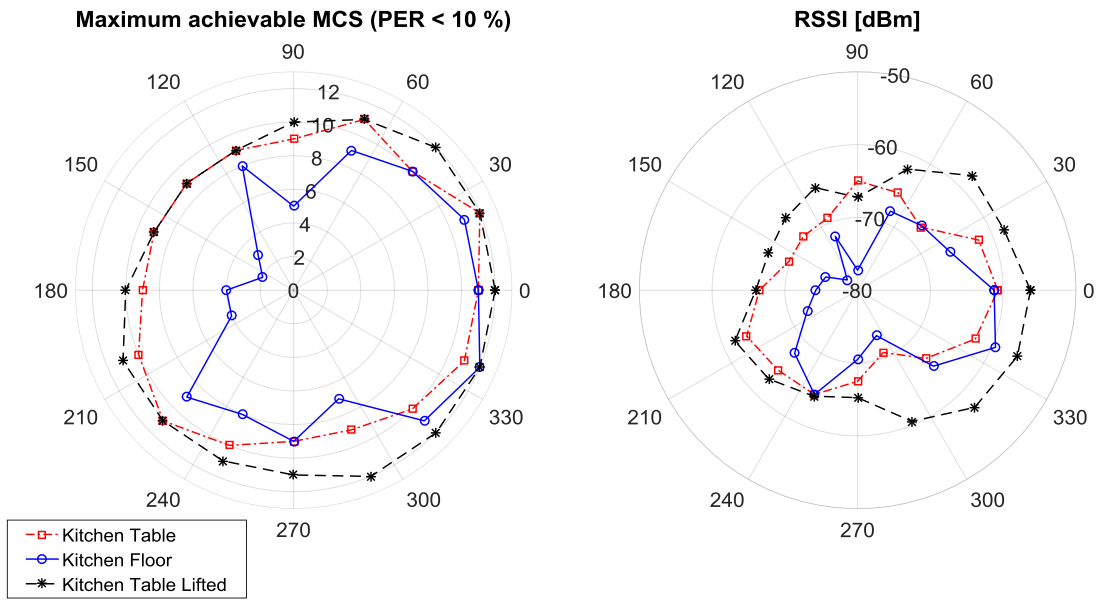

Figure 5.8 *Maximum achievable MCS (left) and measured RSSI (right) as a function of Tx STA yaw angle at measurement points "A", and "C" (see Fig. 4.6).*

Rx STA position and orientation are always the same, except for the kitchen table case when the Rx STA was lifted (similarly as in the earlier section). In addition to that, the results are from the R-FEM that offers better results at the Rx STA.

First, measurements were conducted in the kitchen area. Figure 5.8 combines the results from a top of the kitchen table, on the kitchen floor, and on the kitchen table when the Rx STA was elevated closer to the ceiling. Already from the kitchen table case one can see that the performance of the system is really good at all orientations, and there does not seem to be an orientation where the performance is drastically degraded. The minimum achieved MCS at this location is 9, which equals a throughput of 2.5 Gbps. The lowest measured RSSI value in this location is -70 dBm. Now, the interesting thing is to analyze the used Tx and Rx sectors. In other words, what propagation path does the STA select. In the 0 degrees yaw angle, both STAs select sectors that are pointing towards each other, like they should. Interestingly, at 22.5 degrees orientation the Rx STA performs better with the R-FEM that is not pointing towards the Tx STA and steers the beam to 60 degrees azimuth. In comparison, Tx STA compensates the rotation quite nicely by steering the beam by 20 degrees in azimuth. Another interesting sector selection pair was found at 135 degrees yaw angle, the Rx STA steers the beam by -40 degrees and

the Tx STA by −50 degrees in azimuth. From the CAD model (Fig. 4.5) it can be seen that both the Tx STA and the Rx STA are pointed towards the wall opposite of the Rx STA, meaning that the signal is reflecting from this surface. A clear misalignment for Tx STA's beamformer is found at 270 degrees yaw angle. The Tx STA steers the beam by −60 degrees so that it is pointing to the wall left-hand side of the table. Now, the main beam is basically pointing to the opposite direction from the Rx STA. However, examining the simulated radiation pattern (Fig. 5.2) we see that at 90 degrees azimuth lies the strong sidelobe which is actually pointing straight towards the Rx STA. Hence, one can conclude that the beamforming algorithm is cleverly increasing the actual beam steering range by utilizing the sidelobes which are usually only seen as an impairment and interference. It should be mentioned that in this case the Tx STA would have not been able to steer the beam straight towards the Rx since the angle between these two STAs was 90 degrees and the maximum beam steering angle is 60 degrees. In other yaw angles, the Rx STA chooses sectors that are more or less pointing straight towards the Tx STA, whereas, the Tx STA is constantly looking for new reflecting surfaces. It can also be noticed that the Tx STA is sort of tracking the good reflecting surfaces, such as, the wall opposite of the Rx STA. Overall, it can be said that both STAs are quite good at selecting the LOS path if it is possible, in other words, $|\alpha_{yaw}| \leq \theta_{max}$, where α_{yaw} is the yaw angle ($-180° \leq \alpha_{yaw} \leq 180°$).

The same measurement with the elevated Rx STA gives similar results. Like it was shown in the earlier section, the RSSI values and therefore also the MCS are overall increased when the Rx STA is elevated. Analysis of the Rx beamforming sectors shows that all used sectors have a negative elevation angle. Suggesting that in general the best propagation paths have either LOS or a reflecting surface other than the ceiling. In the Tx side, roughly same reflecting surfaces are used as in the previous case.

Next, the Tx STA was placed on the floor behind the sofa (measurement point "C") to analyze the "worst case scenario" in this kind of a living room environment. It is clear that in this location there is no LOS path available. Surprisingly the RSSI values are not that far away from the Table case when in the range of ±60 degrees yaw from the aligned orientation. In few orientations the performance is actually even better. In these orientations the Tx STA is actually steering the beam to be pointing under the sofa, so that it is actually reflecting from the floor and then perhaps partially penetrating the sofa before finally reaching the Rx STA. Analysis of the selected Tx

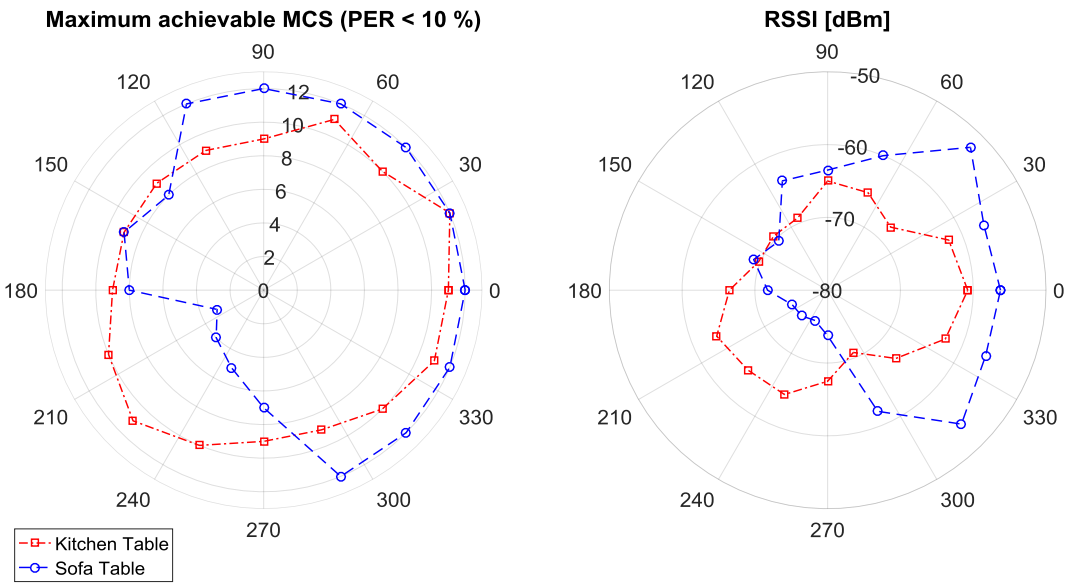

Figure 5.9 *Maximum achievable MCS (left) and measured RSSI (right) as a function of Tx STA yaw angle at measurement points "A" and "B" (see Fig. 4.6).*

sectors reveals that again the wall has been a good reflecting surface and the same "sidelobe trick" has been used to increase the steering range. As an example, at yaw angle of 112.5 degrees the main beam is almost in the optimal orientation to reflect the beam to the Rx STA (hence the peak in the results), whereas, at yaw angle of 157.5 degrees the "sidelobe trick" is used to reflect the sidelobe from the same wall to the Rx STA (hence the low point in the results). An interesting result is found at the yaw angle of 225 degrees where one can see a clear peak. Writer assumes that this peak is caused by the table's metal legs which are of course an excellent reflective surface. However, the legs are relatively thin and seem to not be used as a reflector in other orientations.

Further measurements were carried out closer to the Rx STA. The Tx STA was placed on top of a sofa table (measurement points "B") which is roughly half of the distance than on the kitchen table case (measurement points "A"). Writer assumes that this kind of distances and device placements would be the ones that occur most often in end-user use. The measurement results are shown in Figure 5.9 in blue, and a comparison to the previous kitchen table measurement is shown in red. Intuitively it is obvious that the closer distance yields better results. Furthermore, there are no large objects that would block the LOS path or the Fresnel zones on it, resulting in pretty much optimum channel conditions. The results verify these

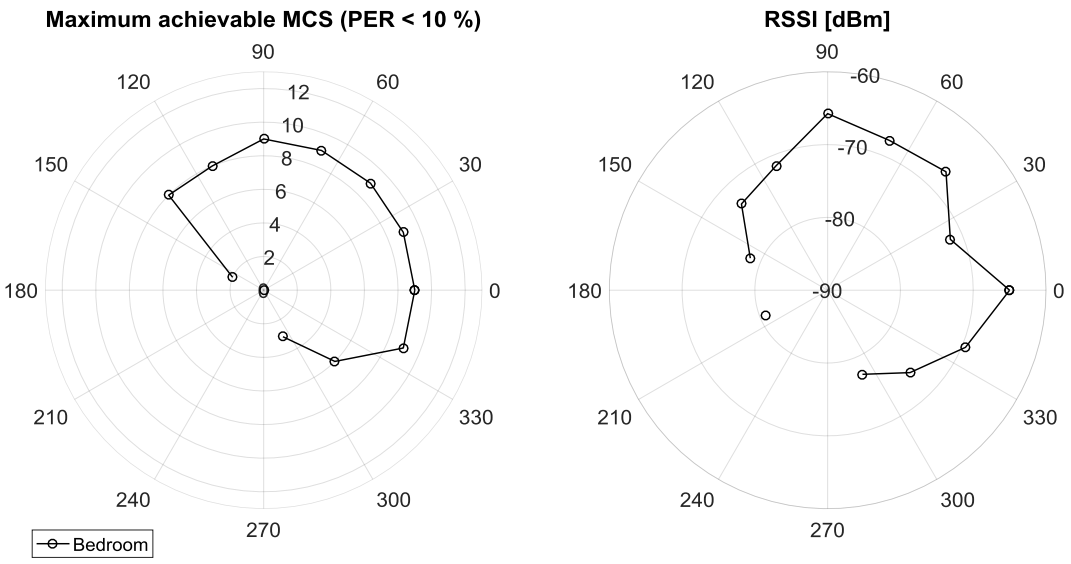

Figure 5.10 *Maximum achievable MCS (left) and measured RSSI (right) as a function of Tx STA yaw angle at measurement points "D" (see Fig. 4.6).*

assumptions: both RSSI and MCS values are higher in the range of −67.5 to 112.5 degrees in yaw. However, surprisingly the results in this location are worse when the Tx STA is pointing away from the Rx STA. There are two large reasons behind this. Firstly, at closer distances it might be difficult to find a good reflecting surface when pointing away from the Rx STA. This limitation can be seen here: even though the windowed wall on the right offers a relatively good reflecting surface, at large yaw angles it cannot be used effectively due to the limited steering angle. Also like mentioned earlier, the quosi-optical signal propagation at these frequencies makes double reflection paths infeasible even at relatively short distances. Secondly, according to our measurements, fabric furniture seem to be relatively easily penetrable but correspondingly offer weak reflective properties. Hence, in our case if the beam is steered towards the sofa placed against the wall, the sofa first introduces some penetration losses, then the wall some reflection losses, and finally again some penetration losses from the sofa. This seems to be the case in our measurements when the Tx STA is steered away from the Rx STA. As the sofa table is so close to the sofa itself, the whole beam steering range of the Tx STA is more or less occupied by the sofa resulting in a poor performance.

Finally measurements were conducted from the bedroom to the living room (measurement points "D"). Unlike in the manual beam steering case, now the Rx STA

was kept in the same location (and orientation) as in the previous beamforming measurements so that the measurements could be compared. The door was also kept closed like it was during the previous measurements in this section. The measurement results are shown in Figure 5.10. This measurement scenario could be described as the "worst case scenario", because not only are the STAs in different rooms but also the Rx STA is aligned away from the Tx STA. Nonetheless, from the results it can be seen that the maximum achievable MCS is above 8 when in the yaw range of $-30°$ to $+135°$. Hence, even in this harsh scenario almost from half of the measurement orientations the theoretical maximum throughput is above 2.31 Gbps. Again, analyzing the utilized sectors reveals few key findings. Again at certain yaw angles, sidelobes of the radiation pattern offer the best performance. An example of this is found at 135° yaw, where the beamformer steers the beam by $-45°$ in azimuth (towards the door). Now, a sidelobe at 70° azimuth is pointing towards the wall behind the bed. It seems that this wall then reflects the beam which then penetrates the non-load bearing wall. Thus, it seems also in this scenario that the sidelobes can be utilized to establish reliable communication links even though the channel conditions are fairly unfavorable. However, when pointing away from the Rx STA (yaw range of 180° to 270°) the whole device discovery seems to fail and communication cannot be established even at MCS 0.

6. CONCLUSIONS

Compared to the past IEEE 802.11 standards, the IEEE 802.11ad takes a completely new approach by operating at the 60 GHz frequency band. The channel bandwidth of 2.1 GHz allows the system to be designed completely differently as high throughputs are achievable with relatively low-complex modulation and coding schemes. However, the high atmospheric attenuation and increased path loss at these millimeter wavelengths force the antenna design to be highly directional. In addition, the high operational frequency and large bandwidth make the circuit level design more challenging. On the other hand, due to these propagation characteristics and highly directional antenna implementations, the interference footprint of these kind of devices is negligible compared to the previous IEEE 802.11 standards. The low interference also means that eavesdropping is much more difficult which of course is highly desirable from the end-user point of view.

In this thesis the objective was to study the performance of an IEEE 802.11ad prototype in a home environment. The previous academic work has mainly focused on measurements in controlled environments, such as, laboratory and office areas. Furthermore, the measurement equipment in these publications is often not explicitly implementing the standard as it would take a great deal of work. In contrast, the measurement setup in this thesis fulfils the requirements of the IEEE 802.11ad standard and implements the Control and SC PHY waveforms (MCS 0–12) as was described in Section 4.1. The measurement scenarios, described in Section 4.2, consisted of measurements inside a room (with and without LOS path) and also a measurement from one room to another. Two types of measurements were conducted: manual beam steering measurements and beamforming measurements. An important observation in the manual beam steering measurements was that not so many household objects are great reflecting surfaces. This is especially important finding as the signal propagation at these frequencies can be described as quosi-optical, that is, the received signal is dominated by the LOS path and the first order reflections. Another key finding was that the rather simple 2x8 phased antenna

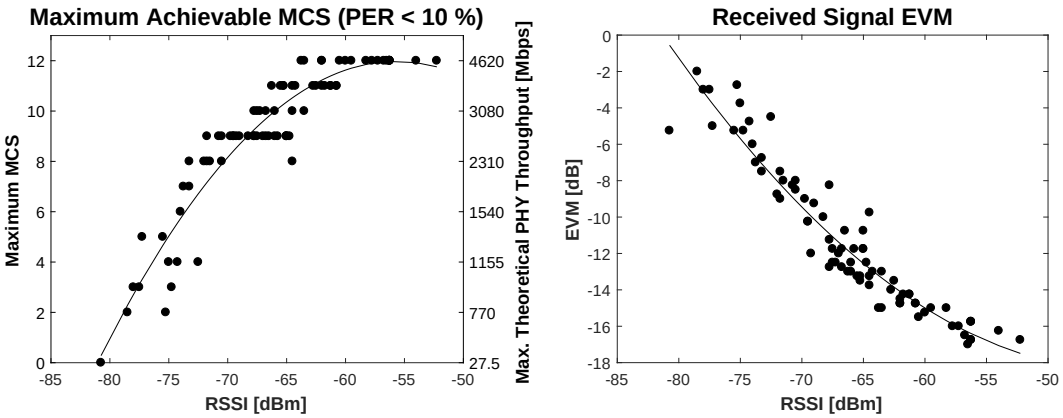

Figure 6.1 *Maximum achievable MCS (left) and EVM (right) as a function of RSSI throughout all beamforming measurements.*

array offers enough directivity and steerability to perform well enough in a typical end-user environment. The beamforming measurements revealed that the utilized codebook and beamforming algorithm perform surprisingly well even in unfavorable measurement scenarios. A summary of these results is shown in Figure 6.1. In over 80 % of all measurements, the maximum achievable MCS is 8 or higher, equaling theoretical throughputs of over 1.925 Gbps. As a comparison, the maximum theoretical throughput of the legacy IEEE 802.11n is just 0.6 Gbps. The variation in the results is due to the variation in the signal quality, for which the EVM is a better metric. From the Figure it can be seen that the EVM can vary considerably for the same RSSI value. Additionally, it can be noticed that the EVM variation decreases when the RSSI increases, which is intuitive. Another contributor to the variations is the delay spread. RMS delay spread characterizes the propagation delays of a channel, and can be used to estimate intersymbol interference [15]. Typical indoor RMS delay spreads at 60 GHz are in the range of $10 - 30$ ns [7]. Importantly, the used MCS selection was purely based on PER. In a consumer product, the link adaptation might be more complex and, for example, could also take into account the EVM and the receiver reported SNR as was described in Section 3.2.

The millimeter wave research is just reaching its golden era. Active study areas include millimeter wave RF circuits, fast ADCs and DACs, millimeter wave antenna arrays, and beamforming algorithms. From this thesis point of view, further studies could be conducted on adaptive antenna arrays and on different codebooks for the switched-beam approach.

REFERENCES

[1] WirelessHD Consortium. *WirelessHD Specification Version 1.1 Overview*. Specification. California, USA, May 2010.

[2] ECMA International. *ECMA-387 (2010), High rate 60 GHz PHY, MAC and HDMI PAL*. Standard. Dec. 2010.

[3] IEEE Computer Society. *Wireless Medium Access Control (MAC) and Physical Layer (PHY) Specifications for high rate wireless personal area networks (WPANs): Amendment 2: Millimeter-wave based alternative physical layer extension*. Standard 802.15.3c. New York, USA: IEEE, Oct. 2009.

[4] IEEE Computer Society. *Local and metropolitan area networks – Specific requirements – Part 11: Wireless LAN medium access control (MAC) and physical layer (PHY) specifications – Amendment 3: Enhancements for very high throughput in the 60 GHz band*. Standard 802.11ad. New York, USA: IEEE, Dec. 2012.

[5] ABI Research. *802.11ad Will Vastly Enhance Wi-Fi – The Importance of the 60 GHz Band to Wi-Fi's Continued Evolution*. White paper, [online], https://www.abiresearch.com/whitepapers/80211ad-will-vastly-enhance-wi-fi/. 2016.

[6] Wi-Fi Alliance. *Wi-Fi CERTIFIED WiGig: Wi-Fi expands to 60 GHz*. White paper, [online], http://www.wi-fi.org/file/wi-fi-certified-wigig-wi-fi-expands-to-60-ghz-2016. 2016.

[7] Hao Xu, V. Kukshya, and T. S. Rappaport. "Spatial and temporal characteristics of 60-GHz indoor channels". In: *IEEE Journal on Selected Areas in Communications* 20.3 (Apr. 2002), pp. 620–630.

[8] A. Maltsev et al. "Experimental investigations of 60 GHz WLAN systems in office environment". In: *IEEE Journal on Selected Areas in Communications* 27.8 (Oct. 2009), pp. 1488–1499.

[9] T. R. Rao et al. "Radio channel characteristics in an indoor corridor environment at 60 GHz for wireless networks". In: *2011 Fifth IEEE International Conference on Advanced Telecommunication Systems and Networks (ANTS)*. Dec. 2011, pp. 1–5.

[10] D. Murugesan and T. R. Rao. “Indoor corridor radio propagation characteristics at 60 GHz for wireless communications”. In: *Computing Communication Networking Technologies (ICCCNT), 2012 Third International Conference on*. July 2012, pp. 1–5.

[11] S. K. Saha et al. “A Feasibility Study of 60 GHz Indoor WLANs”. In: *2016 25th International Conference on Computer Communication and Networks (ICCCN)*. Aug. 2016, pp. 1–9.

[12] A. Lomayev et al. “Experimental investigation of 60 GHz WLAN channel for office docking scenario”. In: *2016 10th European Conference on Antennas and Propagation (EuCAP)*. Apr. 2016, pp. 1–5.

[13] T.S. Rappaport et al. *Millimeter Wave Wireless Communications*. Prentice Hall Communications Engineering and Emerging Technologies Series from Ted Rappaport. Westford, USA: Pearson Education, 2014.

[14] J. du Preez and S. Sinha. *Millimeter-Wave Antennas: Configurations and Applications*. Signals and Communication Technology series. Switzerland: Springer International Publishing, 2016.

[15] T. S. Rappaport, J. N. Murdock, and F. Gutierrez. “State of the Art in 60-GHz Integrated Circuits and Systems for Wireless Communications”. In: *Proceedings of the IEEE* 99.8 (Aug. 2011), pp. 1390–1436.

[16] A. Ghosh. “The 5G mmWave Radio Revolution”. In: *Microwave Journal* 59.9 (Sept. 2016), pp. 22–36.

[17] K. Sakaguchi et al. “Millimeter-wave Wireless LAN and its Extension toward 5G Heterogeneous Networks”. In: *IEICE Transactions on Communications* E98-B.10 (Oct. 2015), pp. 1932–1948.

[18] M. Ayyash et al. “Coexistence of WiFi and LiFi toward 5G: concepts, opportunities, and challenges”. In: *IEEE Communications Magazine* 54.2 (Feb. 2016), pp. 64–71.

[19] Federal Communications Commission. *Amendment of Parts 2 and 15 of the Commission’s Rules to Permit Use of Radio Frequencies Above 40 GHz for New Radio Applications*. Rule proposition Docket 94-124. Washington, D.C., USA, Nov. 1994.

[20] International Telecommunication Union Radiocommunication Sector (ITU-R). *Radio-frequency channel arrangements for fixed wireless systems operating in the band 55.78−66 GHz*. Recommendation F.1497-2. Geneva, Switzerland: International Telecommunication Union, Feb. 2014.

[21] European Telecommunications Standards Institute (ETSI). *The European regulatory environment for radio equipment and spectrum*. Brochure, [online], http://www.etsi.org/news-events/news/379-news-release-30-may-2011. 2011.

[22] European Telecommunications Standards Institute (ETSI). *Broadband Radio Access Networks (BRAN); 60 GHz Multiple-Gigabit WAS/RLAN Systems; Harmonized EN covering the essential requirements of article 3.2 of the R&TTE Directive*. Harmonized European Standard (Telecommunications series) ETSI EN 302 567. Valbonne: European Telecommunications Standards Institute, Jan. 2009.

[23] Finnish Communications Regulatory Authority (Ficora). *Määräys luvasta vapaiden radiolähettimien yhteistaajuuksista ja käytöstä*. Regulation 15 AI/2015 M. Helsinki, Finland: Finnish Communications Regulatory Authority, Dec. 2015.

[24] Agilent Technologies. *Wireless LAN at 60 GHz – IEEE 802.11ad Explained*. Application note, [online], http://cp.literature.agilent.com/litweb/pdf/5990-9697EN.pdf. 2013.

[25] A. F. Molisch. *Wireless Communications*. New York, USA: John Wiley & Sons, 2010.

[26] T. Maseng, R. Landry, and K. Young. "Military communications". In: *IEEE Communications Magazine* 47.10 (Oct. 2009), pp. 36–38.

[27] M. Jacob et al. "Diffraction in mm and Sub-mm Wave Indoor Propagation Channels". In: *IEEE Transactions on Microwave Theory and Techniques* 60.3 (Mar. 2012), pp. 833–844.

[28] S. Saunders and A. Aragón-Zavala. *Antennas and Propagation for Wireless Communication Systems: 2nd Edition*. New York, USA: John Wiley & Sons, 2007.

[29] B. Langen, G. Lober, and W. Herzig. “Reflection and transmission behaviour of building materials at 60 GHz”. In: *Personal, Indoor and Mobile Radio Communications, 1994. Wireless Networks - Catching the Mobile Future., 5th IEEE International Symposium on*. Sept. 1994, pp. 505–509.

[30] H. Zhao et al. “28 GHz millimeter wave cellular communication measurements for reflection and penetration loss in and around buildings in New York city”. In: *2013 IEEE International Conference on Communications (ICC)*. June 2013, pp. 5163–5167.

[31] E. Perahia and M. Gong. “Gigabit Wireless LANs: An Overview of IEEE 802.11ac and 802.11ad”. In: *SIGMOBILE Mobile Computing and Communications Review* 15.3 (Nov. 2011), pp. 23–33.

[32] H. Young and R. Freedman. *University Physics with Modern Physics (13th Edition)*. MasteringPhysics Series. Westford, USA: Pearson Education, 2013.

[33] M. Chryssomallis. “Smart antennas”. In: *IEEE Antennas and Propagation Magazine* 42.3 (June 2000), pp. 129–136.

[34] T. Nitsche et al. “IEEE 802.11ad: directional 60 GHz communication for multi-Gigabit-per-second Wi-Fi [Invited Paper]”. In: *IEEE Communications Magazine* 52.12 (Dec. 2014), pp. 132–141.

[35] Agilent Technologies. *Understanding IEEE 802.11ad Physical Layer and Measurement Challenges*. Training material, [online], http://www.keysight.com/upload/cmc_upload/All/22May2014Webcast.pdf. 2014.

[36] S. Jiang et al. “802.11ad Key Performance Analysis and Its Application in Home Wireless Entertainment”. In: *2014 IEEE 17th International Conference on Computational Science and Engineering*. Dec. 2014, pp. 1595–1598.

[37] Wi-Fi Alliance. *Wi-Fi CERTIFIED Miracast: Extending the Wi-Fi experience to seamless video display*. White paper, [online], http://www.wi-fi.org/downloads-registered-guest/wp_Miracast_Industry_20120919.pdf/7623. 2013.

[38] C. Cordeiro. “Evaluation of Medium Access Technologies for Next Generation Millimeter-Wave WLAN and WPAN”. In: *2009 IEEE International Conference on Communications Workshops*. June 2009, pp. 1–5.

[39] IEEE Computer Society. *Local and metropolitan area networks – Specific requirements – Part 11: Wireless LAN Medium Access Control (MAC) and Physical Layer (PHY) Specifications*. Standard 802.11. New York, USA: IEEE, Mar. 2012.

[40] M. Golay. "Complementary series". In: *IRE Transactions on Information Theory* 7.2 (Apr. 1961), pp. 82–87.

[41] UL Verification Services Inc. *Certification Test Report for Intel 60 GHz Wireless Module Adapter*. FCC certification PD913100NG. Fremont, USA: FCC, Oct. 2014.